RSC Advances

PAPER

View Article Online
View Journal | View Issue

Cite this: *RSC Adv.*, 2025, **15**, 39314

Nanoscale supramolecular complex made of copper cyanide and a phenanthroline ligand inlaid with titanium oxide nanoparticles as effective catalysts and sensors

Safaa Eldin H. Etaiw, *[a] Ibrahim A. Salem,[a] Mona A. Darweesh[b] and Alaa Tawfik [c]

Received 9th September 2025
Accepted 10th September 2025

DOI: 10.1039/d5ra06817g

rsc.li/rsc-advances

Utilizing ultrasonic vibrations, the nano-supramolecular complex $[(phen)_3Cu_2(CN)_3\ (H_2O)_5]$ (NSC**1**) was obtained. NSC**1** was inlaid with nano-titanium oxide to create composite (TiO_2/NSC**1**) nanoparticles using ultrasonic waves. ICP, XRPD, SEM, TEM, TGA, and other spectroscopic methods were applied to characterize the composite. Both NSC**1** and TiO_2/NSC**1** function as heterogeneous catalysts against methylene blue (MB) and brilliant green (BG) dyes, which were assessed and compared. When H_2O_2 is present, it has an effective capacity to degrade (MB) and (BG) dyes. However, the nanocomposite exhibits exceptional degradation efficiency using UV or ultrasonic waves under a variety of conditions. To clarify the mechanisms of mineralization, scavenger techniques, the terephthalic acid disodium salt photoluminescence technique and spectrophotometric titration were used. The TiO_2/NSC**1** nanocomposite's photoluminescence property was analyzed and estimated. So, the composite can ability to operate as a highly efficient selective luminous sensor, which showed outstanding detection and highly effective quenching of the nanocomposite's photofluorescence towards nitrobenzene, Na^+, and Mn^{2+} ions.

1. Introduction

Supramolecular complexes (SCs) can be considered a typical representative of supramolecular chemistry.[1–4] Therefore, they can directly form, under the combined driving forces of noncovalent interactions, varied complex structures with distinct features using various chemical units,[5–8] such as cooperation between metals and ligands,[9] hydrogen bonding,[10,11] host–guest systems,[12] π–π stacking,[13] electrostatic interactions,[14] and van der Waals forces.[15] In addition, several supramolecular complexes have recently garnered increased interest because of their dynamic physical characteristics, such as mechanical, electrical, and optical properties, for applications in the fields of soft robotics and bioelectronics.[16–20] Owing to the unique properties of SCs gained by noncovalent interactions, they are distinguished materials for catalysis,[21–23] sensing,[24,25] artificial light-harvesting,[26] drug delivery,[27] adsorption, separation,[28–32] and other applications.[33]

In recent years, air and water pollution, climate change, and resource depletion have been just a few of the energy and environmental problems caused by the rapid rise in urbanization and industry.[34–37] Thousands of environmental pollutants, including chemical pollutants, often consist of petroleum hydrocarbons, paints, fertilizers, herbicides, hazardous metals, detergents, and dyes. Each category contains many different chemical compounds. The textile and dyeing industries, for example, often employ over 200 thousand commercially available synthetic dyes.[38] Every year, more than 105 tons of industrial effluent is produced by these dyes, which are subsequently thrown directly into streams, rivers, lakes, and even oceans. Many of them are usually non-biodegradable, persistent, and toxic.[39,40]

Additionally, one of the most threatening issues is that some hazardous metals and liquids are found in water resources. As a result, creating effective techniques is essential for such hazardous material detection. Some youth peaple exposed to higher levels of manganese in their drinking water had lower intelligence quotients and more intellectual disabilities. Long-term manganese exposure through breathing naturally occurring manganese in shower water is thought to put a lot of individuals at risk.[41] When hypoxic periods occur, seawater's Mn levels may rise.[42] Different species target specific tissues, including the liver, kidneys, brain, blood, and gills. However, excessive sodium *via* salt is toxic and can result in coma, seizures, and even death. Salt poisoning can cause unconsciousness, convulsions, jitters, and confusion. Fluid changes, brain enlargement, and breathing difficulties can result from a buildup of salt in the blood.[42]

[a]*Department of Chemistry, Faculty of Science, University of Tanta, Tanta, 31527, Egypt. E-mail: safaaetaiw@science.tanta.edu.eg*

[b]*Chemical Engineering Department, Faculty of Engineering, University of Tanta, Tanta, 31527, Egypt*

[c]*Higher Institute of Engineering and Technology, Kafr El-Sheikh, Egypt*

Thus, nowadays, many proposals have been suggested and employed to present a healthy environment for living, but one of them that attracts great attention is heterogeneous photocatalysis because of its low cost and excellent efficiency.[43,44] Nano titanium oxide is one of the most effective photocatalysts, which can be affected by UV-light to generate electron–hole pairs.[45,46] Its wide band-gap energy and high rate of photogenerated charge carrier recombination, however, make it difficult to use in photocatalysis.[47,48]

To solve these issues, many researchers have studied various methods, like nonmetal doping, metal doping of TiO_2, formation of oxygen vacancy, dye sensitization, and semiconductor coupling.[49–53] Some of these tactics are semiconductor pairing with a large surface area, adjustable morphology, and appropriate band placements, which can aid in charge carrier separation, thereby enhancing photoactivity.[54] To achieve this aim, SCs with distinctive characteristics, like structural diversity, porous structures and large surface area, are believed to be the best options.[55] When SCs are inlaid with TiO_2, an aligned core–shell structure is produced, which provides a long optical path length,[56] creating a heterojunction between titania and SCs.

The preparation of nanosized SC and nano TiO_2/SC composites is crucial because they differ from traditional bulk materials in some ways.[57] The self-assembly method for the preparation of NSC**1** and the composite using ultrasonic waves can be considered a powerful tool for obtaining the desired yield within a short time compared with solvothermal techniques, which require high temperatures, high pressures, and lengthy response times. Additionally, the sono-chemical approach is inexpensive, produces numerous results, is an environmentally friendly source and produces a very small size.[58] Therefore, one special homogenization method with several uses is ultrasonication.[59] Large particles in the fluid are typically broken up into uniformly sized particles or smaller fragments by applying sonication.[60,61] By agitating the nanoparticles in the fluid with sound energy, nanoparticles can be produced.[62–65] The ultrasonic effect improves the heat transfer in nanofluids. Therefore, the ultrasonication time and power utilized determine the preparation procedure. However, the exact amount of time and energy required to create nanoparticles using ultrasonography is unknown.

Thus, the current study investigates the synergistic effects of selective sensors derived from phenanthroline and $K_3[Cu(CN)_4]$ that can be inlaid with titanium oxide nanoparticles to form the nanocomposite TiO_2/NSC**1**, which may have more activity and strong power to act as a strong catalyst for the elimination of hazardous materials, such as dyes, and as a selective sensor for some toxic metals and dangerous liquids. Control experiments of NSC**1** and nano-TiO_2 are carried out to compare their catalytic activity along with the synergistic effect of the composite.

2. Experimental

2.1. Materials

All chemicals (phenanthroline, trimethyl tin chloride (Me_3SnCl), potassium cyanide, methylene blue dye and brilliant green dye) and solvents used in the present work are of extremely pure quality and acquired from Merck or Aldrich. $K_3[Cu(CN)_4]$ was prepared as previously reported.[65] The IUPAC name of the methylene blue dye (MB) is 3,7-bis(dimethylamino)-phenothiazin-5-ium chloride, and the brilliant green dye IUPAC name is [4-(diethylamino)phenyl]-phenyl methylidene, Scheme S1.

Organic solvents used include acetonitrile (CH_3CN), dimethyl sulfoxide (DMSO), methanol (MeOH), chloroform ($CHCl_3$), dichloromethane (CH_2Cl_2), tetrahydrofuran (THF), ethanol (EtOH), isopropyl alcohol (IPA), dimethylformamide (DMF), carbon tetrachloride (CCl_4) and nitrobenzene (NB). These solvents are spectroscopic grade BDH. A 30% w/v hydrogen peroxide from Merck was utilized. Using standard $Na_2S_2O_3$, the initial H_2O_2 concentration was determined using the iodometric method.

2.2. Instrumentation measurements

The metal content was recorded using ICP-OES Agilent 5100 Synchronous Vertical Dual View (SVDV), with (VGA7 Serial No. 15150257) Agilent Vapor Generation Accessory. Shimadzu TG-60H and DTA-60H thermal analyzers were used to perform the thermal studies (TGA and DTA) in a nitrogen environment (10 mL min^{-1}) at a heating rate of 10 °C min^{-1}. The Philips pw-1729 (CuKα radiation utilizing Ni filter) and Debye Scherrer pw 1050 (Cu-Kα: Ni-filter) were used to record the powder diffraction patterns of the X-ray. A QUANTA FEG250 microscope was used to take scanning electron microscopy (SEM) pictures of NSC**1** after the gold coating.

2.2.1 Energy dispersive X-ray (EDX). The conventional method for identifying the elemental composition of materials using a scanning or transmission electron microscope (SEM/TEM) is energy dispersive X-ray spectroscopy (EDXS). Energy Dispersive X-ray (EDX) is used instead of EDXS, which is frequently abbreviated. The EDX pictures of NSC**1** were produced using energy-dispersive X-ray spectroscopy (EDX) IT100LA, which is attached to scanning electron microscopy (SEM) and runs at an accelerating voltage of 20.00 keV.

2.2.2 Transmission electron microscopy (TEM). One important analytical technique in the biological, chemical, and physical sciences is transmission electron microscopy (TEM). TEM JEOL JEM-2100 runs at 200 keV of accelerating voltage. TEM photos were viewed, collected, and interpreted using Gatan Digital Micrograph software.

2.2.3 Spectrophotometric measurements. The absorption spectra in the ultraviolet visible region were measured by applying a recording Shimadzu 3101pc spectrophotometer equipped with an electronic temperature controller (Fisher Scientific) (Model 9000).

2.3. Synthesis

2.3.1 Synthesis of nano-supramolecular complex NSC1 and ultrasonic green synthesis of the nanocomposite TiO_2/NSC1. A solution of 99 mg (0.33 mmol) of $K_3[Cu(CN)_4]$ in 30 mL H_2O was combined with a solution of 60 mg (0.334 mmol) of 1,10-phenanthroline (phen) using 20 mL CH_3CN[65] under ambient conditions. The mixture was gently stirred and subjected to

ultrasonic waves. The yellow solution produced green needle crystals after a few hours, which were then washed with H_2O and allowed to dry overnight. Approximately 69 mg of green crystals were obtained. $\mu_{eff.}$ = 1.87 BM. Anal. calc. for NSC**1** ($C_{39}H_{34}N_9O_5Cu_2$): C, 56.0; H, 2.8; N, 15.0; Cu, 15.21%. Found: C, 55.97; H, 2.86; N, 14.92; Cu, 15.29%.

However, nanocomposite TiO_2/NSC**1** was prepared by mixing 1 g of nanosized powder NSC**1** and 0.30 g TiO_2 using ethanol (20 mL), which was dispersed utilizing ultrasonic waves for 45 min, exhibiting 60 W power at 60 °C. The mixture should be stirred for 60 min with heating at 70 °C to aid in the absorption of Ti_2O_3 by NSC**1**. The solution was then illuminated with magnetic stirring for two hours at a wavelength of 365 nm using a high pressure mercury lamp. After filtering off the resultant composite, it was cleaned three times with ionized water, three times with ethanol, and then dried in an oven for twenty-four hours at 70 °C to produce the TiO_2/NSC**1** nanocomposite. Anal cal. For TiO_2/NSC**1** ($TiC_{39}H_{34}N_9O_7Cu_2$): Cu, (calc.) 13.88% (found) 13.64 and Ti, (calc.) 5.23% (found) 5.20.

2.4. Assessment of catalytic activity

For the experiments of catalysis, a stock of MB (2.2×10^{-4} M) and BG dye (2.2×10^{-5} M) was produced in doubly distilled water. A 30% V/V hydrogen peroxide was utilized. $KMnO_4$ solution was used to normalize the H_2O_2 concentration. A range of 25 mL reactors were placed on a water shaker thermostat, a transparent amount of catalyst (0.008 g) and the right amount of dye solution to get 2.2×10^{-4} M methylene blue and 2.2×10^{-5} M brilliant green at ambient conditions. Two milliliters of 0.2 M H_2O_2 were added to each reactor, and the time was noted. An aliquot was collected from each reactor at predetermined intervals, and the MB dye's absorbance was recorded at 665 nm, while the BG dye's absorbance was observed at 625 nm.

2.5. Photocatalytic activity measurements

The degradation of MB and BG dyes under ambient conditions was examined through an investigation of catalytic activity. After 60 minutes in the dark at 28 ± 1 °C, the water shaker thermostat was used to store the solutions to achieve equilibrium between adsorption and desorption. The photocatalytic activity was conducted utilizing a 300 W medium pressure mercury lamp at λ = 365 nm under UV light radiation. The reactor was placed in an ultrasonic bath to examine the effect of sonication on dye mineralization. The experiments were conducted using standard procedures comparable to those used under ambient conditions. Throughout the radiation process, at regular intervals, an aliquot was removed from each flask, and the absorbance was recorded.

In the control experiment, identical steps were conducted without the use of a catalyst. To optimize the reaction parameters used to conduct the reaction by varying one while keeping the others constant, the impact of reaction conditions, specifically the pH of the medium, the H_2O_2 concentration, the concentration of dye, and the dosage of the catalyst, was investigated. In general, it was discovered that for a few hours, the dye/H_2O_2 mixture stayed steady without causing any variations in absorption. In addition, control experiments on the effects of nano-TiO_2 and NSC**1** catalysts on the degradation of the dyes were investigated to compare the advantages of the composite.

Additionally, the catalytic activity of the catalysts was tested under the same conditions as ammonium oxalate (AO) and isopropanol (IPA). In addition, the spectrophotometric titration of MB dye by isopropanol under optimum conditions was carried out to identify the active species during the catalytic reaction.

The formula for calculating the catalytic degradation efficiency (D%) was

$$D\% = \{(A_0 - A_t)/A_0\} \times 100. \quad (1)$$

In this case, A_t represents the dye's residual absorbance at time t and A_0 represents its initial absorbance at time 0.

2.6. Photoluminescence sensing measurements

Ten milliliters of several chemical solvents, including MeOH, DMSO, $CHCl_3$, CH_2Cl_2, THF, EtOH, IPA, CH_3CN, DMF, CCl_4, and nitrobenzene (NB), are used to suspend 5 mg of finely ground TiO_2/NSC**1** by ultrasonic radiation, and after that, measurements are made of the fluorescence spectra of suspensions in different solvents. To conduct the sensing tests, 5 mg of TiO_2/NSC**1** is dispersed in H_2O with a fixed concentration of $M(NO_3)_n$ (1×10^{-3} mol L^{-1}) M = Cd^{2+}, Hg^{2+}, Ag^+, Ni^{2+}, Sn^{2+}, Cu^{2+}, Co^{2+}, Fe^{2+}, K^+, Mn^{2+}, and Na^+. After 10 minutes of ultrasonic treatment, the suspension is excited at 360 nm, and the associated fluorescence intensity is measured at room temperature. To detect hazardous liquids and metal ions, this is done to study the luminescence behavior of TiO_2/NSC**1** as a selective sensor.

3. Results and discussion

3.1. Structure of (NSC1) and the composite TiO_2/NSC1 nanoparticles

Utilizing the self-assembly approach, NSC**1** was obtained using phenanthroline and K_3[Cu (CN)$_4$] in a water/acetonitrile solution using ultrasonic radiation. The straightforward technique avoids the high pressure and temperature needed for the solvothermal approach. NSC**1** is easily soluble in organic solvents but air stable and insoluble in water. Elemental analysis supports the chemical formula $C_{39}H_{34}Cu_2N_9O_5$, and single-crystal X-ray analysis verified NSC**1**'s chemical composition $[Cu^I(CN)(phen)_2Cu^{II}(CN)_2(phen)]\cdot 5H_2O$.[66] Table S1 presents the crystal data for NSC**1**. The structure of NSC**1** indicates the presence of two mixed valence two copper complexes in addition to H_2O (Fig. 1). An asymmetric unit of NSC**1** shows the Cu^I complex, which coordinates two phen units *via* nitrogen atoms and one cyanide group adopting a distorted trigonal bipyramid (TBPY-5) structure, Fig. 1 and Table S2. The H-bonds (2.73–3.27 Å) binding the C≡N ligands to water molecules are the cause of the divergence of the (TBPY-5) structure. Few Cu^I complexes containing TBPY-5 geometry are known.[67–69] The initial class of complexes containing trigonal pyramidal copper(I) with a low

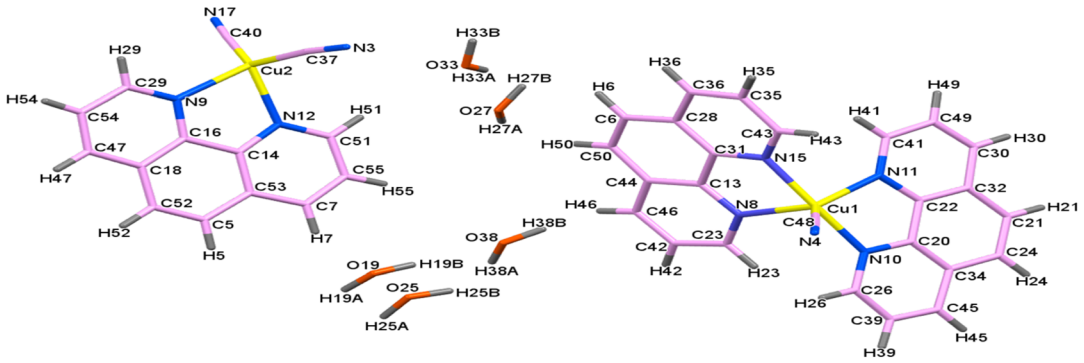

Fig. 1 Asymmetric unit of NSC**1** with an atom labeling scheme.

electron density methyl acrylate was recently believed to be copper(I)/2,2-bipyridine complexes.[70] In addition, complex cations $[CuL_2]^{2+}$ containing N_3O_2 polyhedron crest a trigonal bipyramid.[71]

Moreover, the asymmetric unit contains a crystallographically different Cu^{II} complex, which coordinates to the nitrogen atoms of a phen molecule and 2 CN-groups, creating a slightly distorted tetrahedron (T-4), Table S2. Several compounds containing the Cu^{II} ion have deformed tetrahedral geometry, some of which are biologically significant.[72–74] Tetra coordinate complexes may create tetrahedral or square-planar topologies whose two planes, each containing copper and two nearby donor atoms, subtend an angle, allowing its identification. In T-4 complexes exhibiting D_{2d} symmetry, the tetrahedrality is 90°. However, tetrahedrality is equivalent to zero in square-planar complexes with D_{4h} symmetry. The two planes in NSC**1** (C37Cu2C40 and N12Cu2N9) have an angle of 86.22, which supports Cu^{II}'s tetrahedral geometry.

The asymmetric unit also contains five H_2O molecules that are quite significant in pecking the structure of NSC**1**. Careful investigation of crystal packing indicates that H_2O molecules are assembled *via* H-bonds (1.92–2.96 Å), and because of the brief interactions between the oxygen atoms, they are closely packed (2.76–2.87 Å) by π–π interactions to create a 1D water cluster ribbon.[66]

When constructing supramolecular structures, cyanometallates help build components *via* M–CN–M bridging linear coordinate bonding interactions. However, it is uncommon to find cyanide as a terminal ligand that can act as an acceptor of hydrogen bonds.[75] The most interesting aspect of NSC**1**'s structure is the large number of supramolecular interactions, such as π–π stacking and H···N–C hydrogen bonds, which create a distinctive 3D supramolecular architecture in the solid state, Fig. S1. Furthermore, the water molecules disperse among the Cu^{I} and Cu^{II} fragment layers to create H-bonds between the H-atoms and terminal cyanide groups of phen ligands to enlarge the NSC**1** structure into a 3D-network, Fig. S1. Therefore, extensive hydrogen bonds, π–π interactions and short contacts play a role in the strong backing of the structure of NSC**1**.

It is crucial to remember that there are no Cu–Cu interactions because of the shortest distances between Cu1–Cu1 = 7.599 Å, Cu2–Cu2 = 12.692 Å and Cu1–Cu2 = 6.137 Å. Conversely, NSC**1**'s structure is made up of distinct neutral molecules with separation distances that are significantly greater than those of an ionic bond. In the case when no ionic contact occurs, the smallest distance between any two close Cu^{I} and Cu^{II} atoms is 6.137 Å, even though the distances between the two CN ligands of the $[Cu^{II}(phen)(CN)_2]$ complex and the Cu atom of the $[Cu^{I}CN(phen)_2]$ complex are N3–Cu1 = 5.803 Å and N17–Cu1 = 5.625 Å, respectively.[76]

A mixture of 1 g of nanosized powder NSC**1** and 0.30 g nano-TiO_2 using 20 mL ethanol was dispersed utilizing ultrasonic waves to produce the nano-composite TiO_2/NSC**1**. Following a review of the XRD simulated plot of NSC**1**, Fig. 2 displays the X-ray powder diffraction (XRPD) of nano-TiO_2, NSC**1**, TiO_2/NSC**1** composite, and the recycled TiO_2/NSC**1** composite. At $2\theta = 24°$, 30°, 34°, and 45°, the TiO_2 XRD pattern shows four modest intensity indications. However, NSC**1** clearly matches the simulated pattern obtained from the XRD of the single crystal of NSC**1**, demonstrating the phase purity of the bulk sample of NSC**1**. Additionally, the XRD pattern of the composite shows most of the signals of the simulated pattern in addition to those of TiO_2, especially the signal at 24°, while the others exhibit weak intensity. In addition, XRPD supports the ability of the composite to maintain its identity and stability throughout the catalytic processes, as demonstrated by the composite's XRPD after recycling, Fig. 2e.

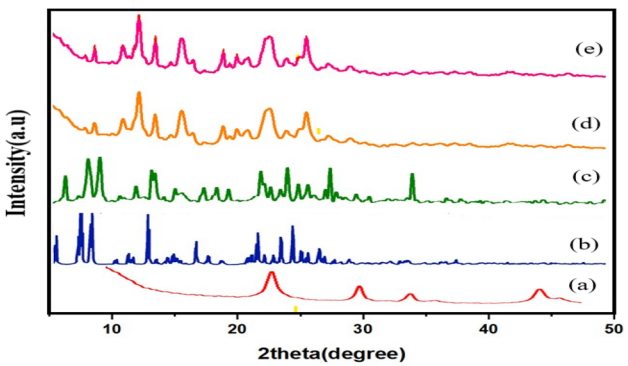

Fig. 2 XRBD patterns of (a) TiO_2, (b) simulated NSC**1**, (c) NSC**1** experimental, (d) TiO_2/NSC**1** composite fresh, and (e) TiO_2/NSC**1** recycled.

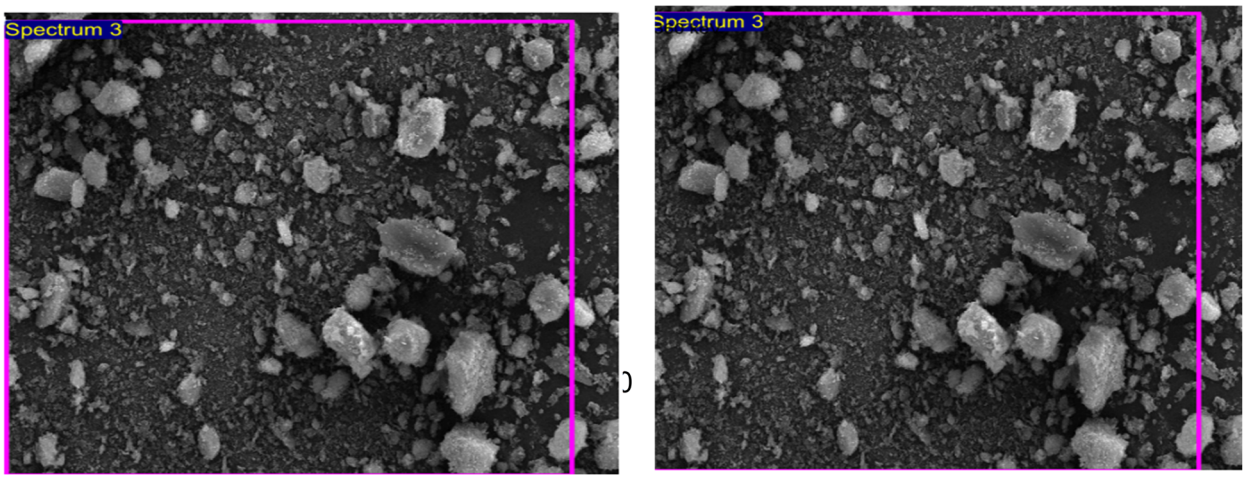

Fig. 3 SEM images of the TiO_2/NSC**1** composite.

Scanning electron microscopy (SEM) pictures reveal details about the sample's composition and surface topography. The TiO_2/NSC**1** composite appears to be large gray granules exhibiting different shapes in addition to many smaller particles, Fig. 3. It is observed that there are some bright circular spots on the surface of the granules, indicating the inclusion of the TiO_2 in the structure of the composite. This opinion is also supported by energy dispersive X-ray (EDX) images, which determine the composition of the composite. The EDX images indicate the presence of Cu (at 1.8 and 8.8 keV), Ti (at 0.04, 4.06 and 5.0 keV), O_2 (at 0.05 keV) and carbon, Fig. 4. However, transmission electron microscopy (TEM) images of NSC**1** exhibit circular black nanostructures with the size of the particles in the range of 41–76 nm, Fig. 5a. Meanwhile, the morphology of the composite shows black rods with bright white parts with nano dimensions equal to 20.60–33.89 nm (Fig. 5b).

3.2. Spectroscopic characteristics of NSC1 and TiO_2/NSC1 composites

The stretching vibrations of H_2O molecules are represented by a noticeable band at 3400 cm^{-1} in the NSC**1**'s infrared spectrum, Fig. S2. The unique bands of the phenanthroline ligand and the $(CuCN)_n$ fragment are also visible in the infrared spectrum. The bands of the phenanthroline ligand are visible in the spectra at 3060, 2930 cm^{-1} (υ_{CHarom}), 1420 cm^{-1} (δ_{CH}), and 770, 724 cm^{-1} (γ_{CH}). The hydrogen bonds forming between the donor sites of the $(CuCN)_n$ fragment cause the hydrogen atoms in the ligand to shift to lower wave numbers from the vibration frequencies of the free phen ligand.[77] The C=C bonds of **1** phen ligands are responsible for the bands at 1585, 1508, and 1460 cm^{-1}, while the band at 1609 cm^{-1} is associated with $\nu_{C=N}$. These bands help phen coordinate Cu centers and show slight shifts to lower wave numbers from those of the phen molecule. The NSC**1** spectrum shows the IR bands at 2130 and 2085 cm^{-1}, which support two different cyanide groups. The fact that the first type of cyanide group is connected to Cu^{I} and the second is coordinated to the Cu^{II} center supports the existence of a coordination polymer of mixed valence copper cyanide. Additionally, the Cu–C bands at 430 and 436 cm^{-1} confirm the existence of two $(CuCN)_n$ components (Fig. S2).

Since the spectrum of 1,10-phenanthroline, shown in Fig. S3 and Table S3, is similar to the spectra of naphthalene, phenanthrene, and anthracene, it must be considered when discussing the electronic absorption spectrum of NSC**1**. Similar to naphthalene, 1,10-phenanthroline exhibits very minor spectroscopic alterations when nitrogen is substituted for methane (Table S3 and Fig. S3). The $^1Ba \leftarrow {}^1A$ transition is attributed to the phenanthroline wavelength band, which peaks at 200 nm. The phenanthroline spectrum at 224 nm is like the longitudinally polarized $^1B_b \leftarrow {}^1A$ band at 225 nm.[77] The ^1L_a and ^1L_b bands appear at the normal positions at 265 and 285 nm, respectively. Compared to the spectra of anthracene (310 nm) and naphthalene (286 nm), this band shows a blue shift.[77] In contrast, the NSC**1** spectrum shows the same phenanthroline bands at about the same locations (Table S3 and Fig. S3). Along with a broad band at 307 nm corresponding to O 2p → Ti 3d transition of TiO_2, the UV spectrum of the TiO_2/NSC**1** composite resembles that of NSC**1**, exhibiting a slight blue shift in the ^1L_a and ^1L_b bands (Table S3 and Fig. S3), which supports that TiO_2 should be included in the NSC**1** network, Fig. S3.

Although the unaltered phen is known to be a weakly emissive substance, a variety of highly luminous phenanthroline compounds with emission bands spanning from the ultraviolet to the near-infrared region can be created by taking different approaches.[78] The emission primarily comes from the n–π* and π–π* singlet excited states, which are closely located in the phenanthroline.[79,80] n–π* excited states are typically characterized by vanishingly low emission quantum yields and frequently decay *via* non-radiative paths. At ambient temperature, phenanthroline has a brief lifespan for the singlet (t < 1 ns) and a poor fluorescence quantum yield ($\theta_{fl} = 0.0087$).[78] According to Table S3 and Fig. S4, the emission spectrum of phenanthroline in DMF shows a very weak band at 555 nm, two shoulders at 380 and 425 nm, and a clear peak at 365 nm. The last three structured bands indicate the close-lying π–π* transition. The concentration dependence of the delayed emission band at

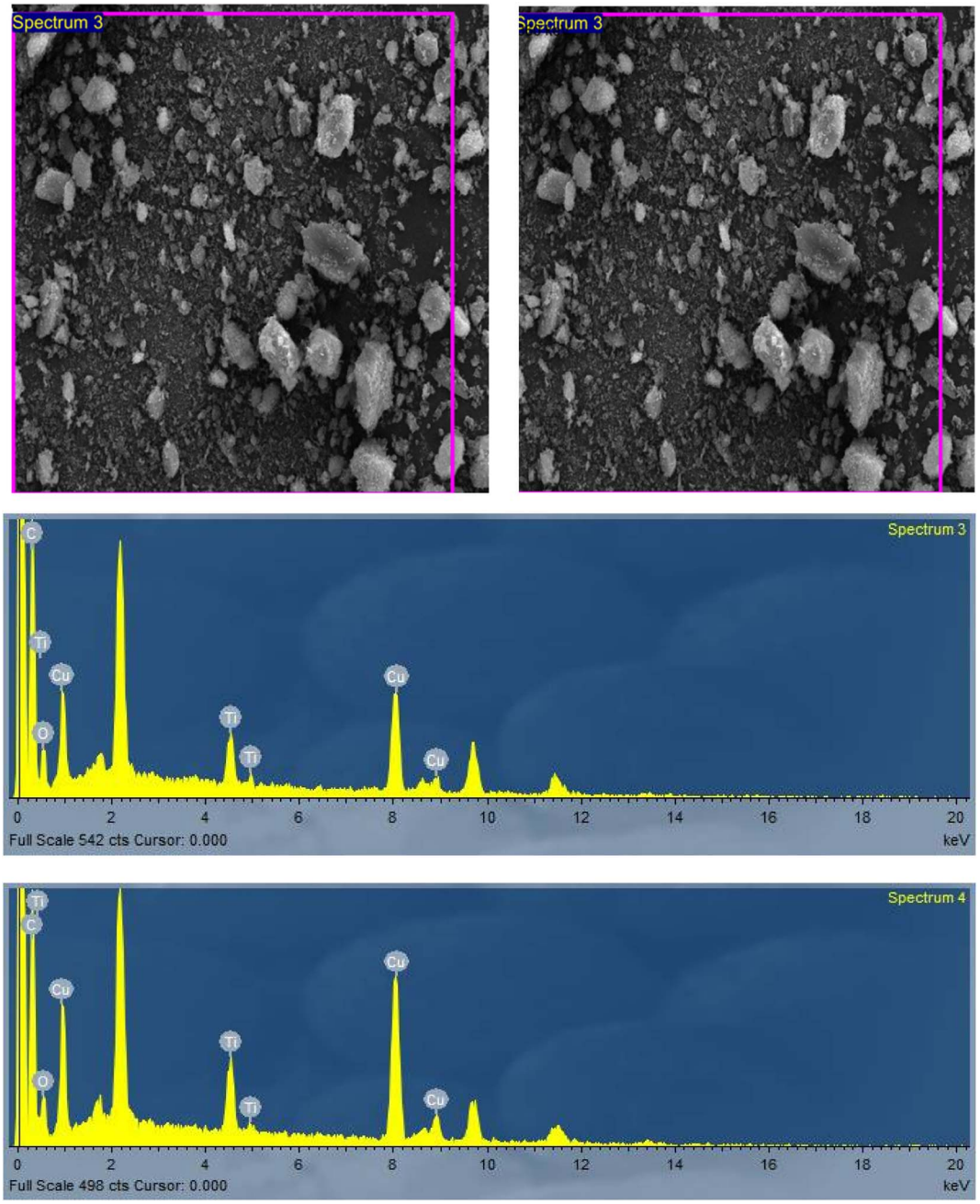

Fig. 4 EDX images of the TiO_2/NSC**1** composite.

555 nm confirmed that the triplet excimer of phen was attributed to this low-energy, delayed emission band. The excimer phosphorescence of phenanthroline, quinoxaline, and naphthalene provided more evidence for this classification.[81,82]

There is a broad band at 365–392 nm containing faint shoulders in the emission spectrum of NSC**1**.[83] The close-lying π–π* transition is represented by these structured bands.[82] Both the phen ligand and the CuCN fragment, which glow at λ_{max} = 392 nm, are present in the structure of NSC**1**.[82] The visible spectrum emission of CuCN compounds containing amines was found, and their photophysical behavior appears to be similar to that of CuCN.[84] The transition between the ground state and the lowest triplet excited state is believed to be the source of the CuCN emission spectrum. Additionally, the comparatively high energy CuCN emission is believed to be caused by a bent triplet state.[85] However, the creation of the NSC**1** allows for the tuning of both the photophysical characteristics of phen and CuCN. The composite and NSC**1**'s emission spectra show a broad band with a 375 nm core. This band results from the So–T transition in the CuCN fragments, which shifts to a wavelength that is about 30 nm longer than that of the CuCN. The broad band at 365 nm displays the coordinated Phen's near-lying π–π* transitions (Table S3 and Fig. S4). Therefore, TiO_2/NSC**1** composite is a desirable luminescent

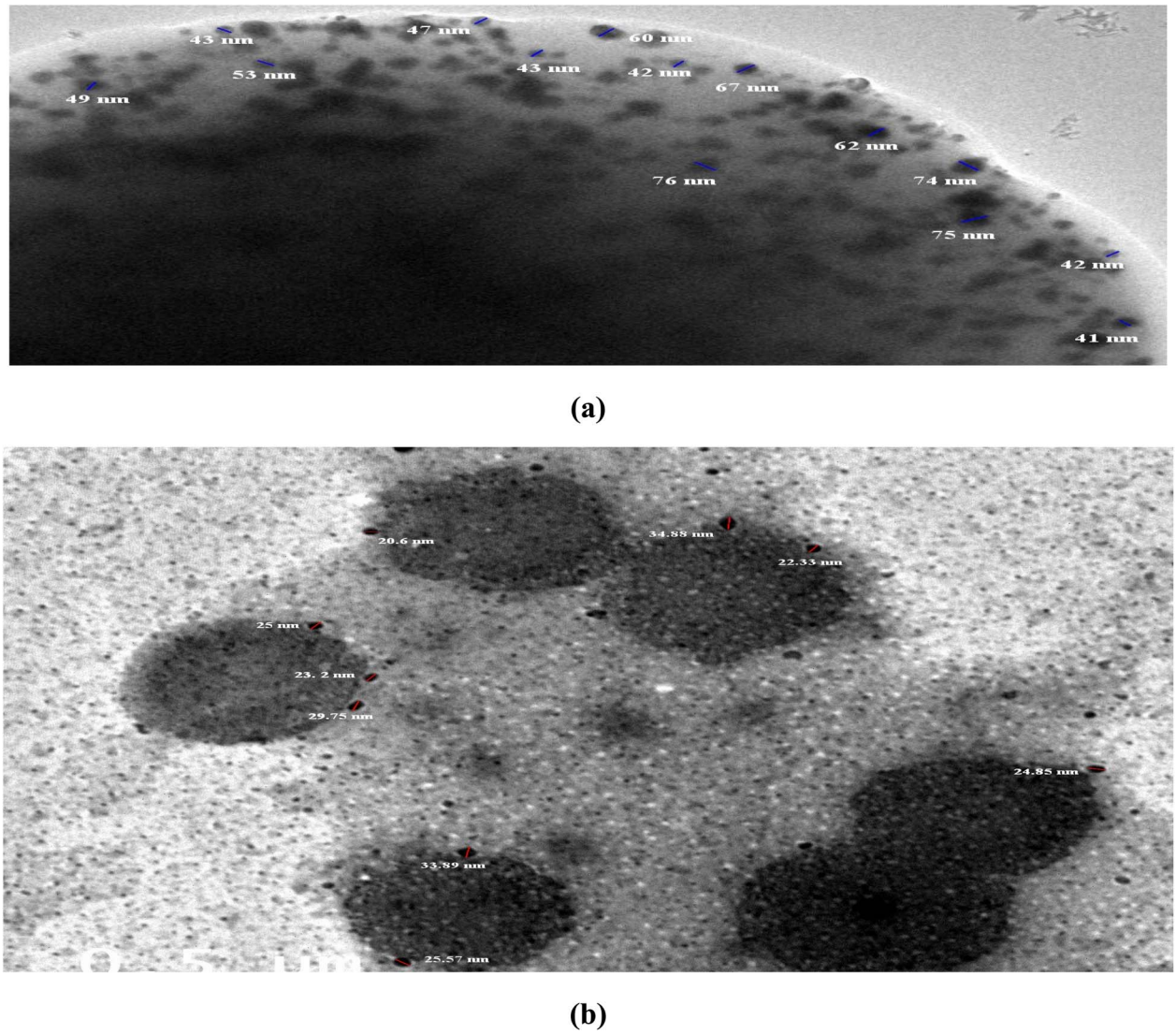

Fig. 5 TEM images of NSC**1** (a) and the TiO_2/NSC**1** composite (b).

sensor due to its great sensitivity to some metals and organic liquids in its luminescence characteristics. Nevertheless, band broadening makes it impossible to rule out the possibility of single-metal-centered (MC) transitions of the types $3d^{10} \rightarrow 3d^9 4s^1$ and $3d^{10} \rightarrow 3d^9 4p^1$ on the metal to ligand charge transfer (MLCT) (high energy band) and the Cu(I) center (low energy bands).

3.3. Thermogravimetric analysis

Thermogravimetric analysis, or TGA, curve analysis tells us how much a sample's mass changes with temperature and time. It is employed to assess oxidative stabilities, temperature transitions, and material composition. The NSC**1** and TiO_2/NSC**1** thermograms all show four stages of disintegration (Fig. S5 and S6, Table 1). At 85–155 °C, five water molecules are liberated in the first step. Δm% obser 10.48 (calc.) (10.67). In step two, the first phen molecule is removed using Δm% obser at 157–247 °C. Calc. at 21.12 obser, (21.48). Step 3 in the temperature range of 252–505 °C reveals the release of the remaining phen molecules, Δm% obser. (calc.) 42.49 (43.08). According to Δm% obser, the disintegration of 3 CN ligands is what causes the weight loss at 507–648 °C. Obser. (9.22) and 9.8 (calc.). The residue's molecular weight matches that of metallic copper after NSC**1** has been fully thermolyzed in a nitrogen environment, as indicated by mass% obser. 23.94 (calc.) 23.62, Table 1.

Although phen ligands are developed at relatively high temperatures, the NSC**1**'s thermogravimetric investigation reveals that its structure contains stable $Cu^{I,II}$–CN chains that can withstand temperatures of up to 620 °C. This implies that hydrogen bonds hold the phen molecules together in the 3D network and that they are highly coordinated *via* Cu atoms. Furthermore, the fact that H_2O molecules first released up to 85 °C implies that they are not in coordination with Cu atoms. For the full discharge of H_2O, this temperature can exceed 155 °C, which signifies the creation of H-bonds that must be broken at a relatively high temperature. However, as shown in Fig. S6, the TGA curve shows four endothermic stages for the composition of the nano TiO_2/NSC**1** composite.

Table 1 Thermogravimetric analysis data of NSC**1** and the TiO_2/NSC**1** composite

NSC**1**	Step	Temp. range (°C)	Δ*m* (%), obs.	Δ*m* (%), cal.	Assignment
	1	85–155	−10.48	−10.67	-5(H_2O)
	2	157–247	−21.12	−21.48	-(Phen)
	3	252–505	−42.49	−43.08	-2(phen)
	4	507–648	−9.22	−9.28	-3(CN)
	Residue	Temp. range (°C)	$Mass_{obs}$ (%)	$Mass_{cal}$ (%)	
	3Cu%	Over 700	23.62	23.94	3Cu%
TiO_2/NSC**1**	Step	Temp. range (°C)	Δ*m* (%), obs.	Δ*m* (%), cal.	Assignment
	1	60–130	−10.62	−10.59	-5(H_2O)
	2	200–290	−21.10	−21.19	-(Phen)
	3	300–470	−42.93	−42.28	-2(phen)
	4	490–620	−9.10	−9.12	-3(CN)
	Residue	Temp. range (°C)	$Mass_{obs}$ (%)	$Mass_{cal}$ (%)	
	Cu + TiO_2	620–780	16.23	16.59	Cu + TiO_2%

NSC1 and the TiO_2/NSC**1** composite thermogram are represented in Fig. S6 and Table 1, all show four stages of disintegration. In the first stage, five water molecules are liberated at 60–130 °C, Δ*m*% obser. 10.62 (10.59) (calc.). One phen ligand is removed in the 2nd step at 200–290 °C, Δ*m*% obser. 21.10 and (21.9) (calc.). The 3rd phase at the temperature range of 300–470 °C is caused by the release of the other two phen ligands, Δ*m*% obser. (calc.) 42.93 (42.28). At 490–620 °C, the three cyanide groups dissolve as cyanogen, which causes weight loss, or Δ*m*% obser. (calc.) = 9.10 (9.12). Mass% observe indicates that the residue's molecular weight matches that of metallic copper and TiO_2 after the composite has been fully thermolyzed. 16.23 (16.59) (calc.), Table 1.

3.4. NSC1 and TiO_2/NSC1 composite's catalytic and photocatalytic properties

The textile industry's wastewater contains significant amounts of organic compounds, which increase the toxicity of the effluents. It is commonly known that due to their excellent endurance and aromaticity, azo dyes cannot be mineralized using conventional aerobic biological treatment techniques. The development of more economical and environmentally friendly alternatives to traditional techniques for the degradation of organic pollutants is therefore of great interest now.[86,87] In practically every production sector, H_2O_2 is employed extensively, especially in the chemical industry and environmental protection.[88] It has made a substantial contribution to ecologically friendly chemical industry operations because water is a unique byproduct of its use. A series of chemical treatment techniques known as advanced oxidation processes (AOPs) is intended to eliminate organic (and occasionally inorganic) contaminants from water and wastewater by oxidation through interactions with hydroxyl radicals (˙OH).[89] However, this term more accurately describes a subset of these chemical processes that employ UV radiation, hydrogen peroxide (H_2O_2), and ozone (O_3), or a combination of the few techniques, in actual wastewater treatment applications.[90] Using methylene blue (MB) and brilliant green (BG) as illustrative examples, the catalytic behavior of NSC**1** and TiO_2/NSC**1** was investigated in the presence of H_2O_2 as an environmentally acceptable environment. Under normal environmental conditions, these colors remain stable, and waste streams have a hard time breaking them down. The MB and BG dye spectra at 660 nm and 625 nm, respectively, are used to monitor the degradation tests. Even after extended periods of 24 hours, the spectra of MB and BG dyes exposed to UV light exhibit only a slight discernible decrease in the strength of the distinctive bands. However, the initial spectra experiments, which were near H_2O_2 in dim, show that in 0–240 min, there are minor changes in the absorption intensity of dyes; meanwhile, reasonable degradation efficiencies need long times, Fig. S7 and S8. Therefore. MB and BG dyes resist H_2O_2 degradation in the absence of a catalyst. In this instance, catalyst NSC**1** and H_2O_2 (normal circumstances) must be present when the MB and BG dyes degrade, Table 2.

Under normal conditions, the absorption peaks of MB and BG clearly lose intensity when H_2O_2 and NSC**1** or TiO_2/NSC**1** catalysts are present. When BG is used with the NSC**1** catalyst, the *D*% is 97.63 in 62 minutes; however, the TiO_2/NSC**1** composite has a significantly higher degrading efficiency than NSC**1** (*D*% is 98.95 in 40 minutes), Table 2. However, BG dye's spectra employing the TiO_2/NSC**1** composite indicate that *D*% = 98.95% within 40 minutes, suggesting that it is more resistant to mineralization than MB (Table 2).

Furthermore, Fig. 6a and b demonstrate that the composite is more effective at mineralizing the dyes than NSC**1**. For example, MB exhibits a degradation efficiency of 98.93% in just 24 minutes, while NSC**1** displays a mineralization efficiency of 98.80% in 42 minutes. Additionally, to assess the synergistic effect of the current catalysts, the catalytic activity of nano-TiO_2 on methylene blue dye was investigated. The nano-TiO_2 catalyst exhibits a long time (120 min) to mineralize 60.6% MB dye, Table 2 and Fig. S9.

3.5. Operating condition impact on the degradation of MB dye

Determining which variables have the largest effects and the values that produce the most dependable performance is essential for

Table 2 Kinetic parameters of catalytic degradation of brilliant green (BG) and methylene blue (MB) using NSC**1** and TiO_2/NSC**1** catalysts[a]

System	D (%)	Time (min)	k_{obs} (min^{-1})	R^2
Brilliant green (BG)				
BG + UV-light	77.48	360	0.0059	0.992
BG + H_2O_2	96.8	240	0.0017	0.991
NSC1				
BG + NSC**1** + H_2O_2 (NC)	97.33	62	0.056	0.988
BG + NSC**1** + H_2O_2 + UV-light	99.9	28	0.092	0.88
BG + NSC**1** + H_2O_2 + ultrasonic waves	93.2	15	0.2	0.95
TiO_2/NSCP1				
BG + TiO_2/NSCP**1** + H_2O_2 (NC)	98.95	40	0.125	0.987
BG + TiO_2/NSCP**1** + H_2O_2 (OC)	96.33	20	0.1490	0.981
BG + TiO_2/NSCP**1** + H_2O_2 + UV-light	99.9	15	0.324	0.718
BG + TiO_2/NSC**1** + H_2O_2 + ultrasonic waves	93.2	6	0.394	0.967
Methylene blue (MB)				
MB + UV-light	90.62	(h)24	0.0020	0.99
MB + H_2O_2	95	(h)24	0.0020	0.99
NSC1				
MB + NSC**1** + H_2O_2 (NC)	98.8	42	0.073	0.953
MB + NSC**1** + H_2O_2 + UV-light	97.5	55	0.06	0.96
MB + NSC**1** + H_2O_2 + ultrasonic waves	97.3	14	0.191	0.86
TiO_2/NSCP1				
MB + TiO_2/NSCP**1** + H_2O_2 (NC)	98.93	24	0.178	0.953
MB + TiO_2/NSCP**1** + H_2O_2 (OC)	97.43	12	0.324	0.9673
MB + TiO_2/NSCP**1** + H_2O_2 + UV-light	97.97	5	0.793	0.793
MB + TiO_2/NSCP**1** + H_2O_2 + ultrasonic waves	97.5	3	0.0133	0.999
TiO_2	60.6	120	0.007	0.93

[a] (NC) = normal conditions = (BG = 2.2×10^{-5} M), (MB = 2.2×10^{-4} M), (0.2 M) H_2O_2 as oxidant, pH = 6.5 and (0.001 g) NSC**1**, and (0.001) g TiO_2/NSC**1** composite. (OC) = optimum conditions: (BG = 2.2×10^{-5} M), (MB = 2.2×10^{-4} M), (0.2 M) H_2O_2 as oxidant, pH = 6 and (0.008) g TiO_2/NSC**1** composite.

optimizing the design of an existing process. The amount of H_2O_2, scavenging agents, pH, dye concentration, catalyst dosage, and other variables have an impact on degradation efficiency.

The initial H_2O_2 concentration, which ranges from 0.02 to 0.5 M, has a substantial impact on the rate of degradation of MB dye (Fig. S10, 7 and Table 3). The initial reaction rate increases

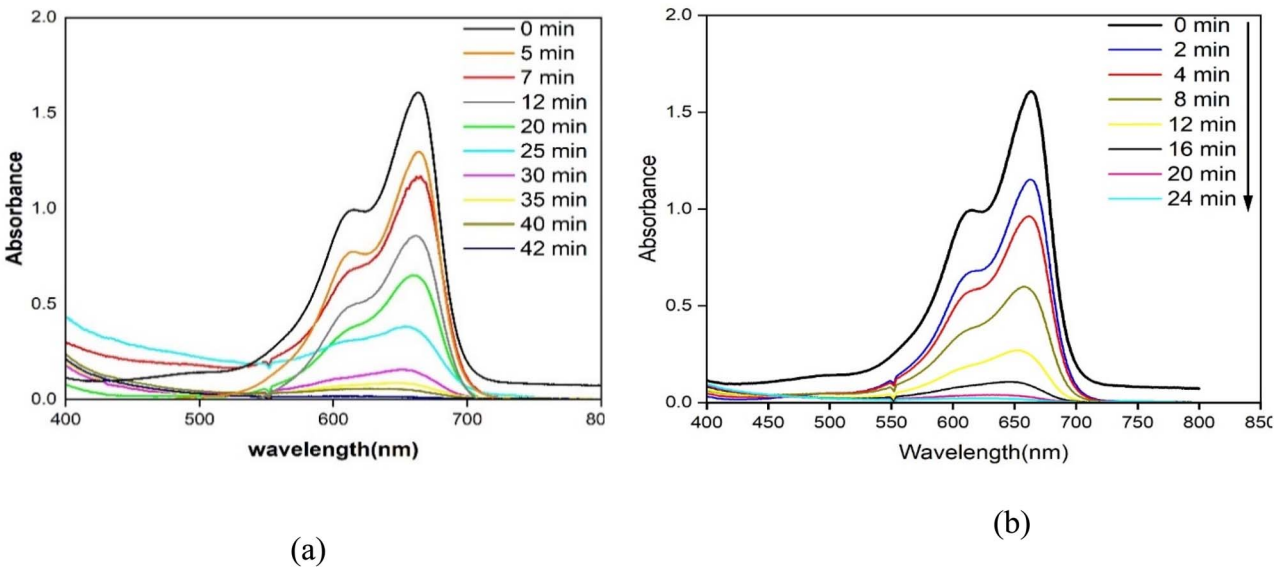

Fig. 6 Spectra illustrates the electronic absorption of the MB dye solution's mineralization (2.2×10^{-4} M) and (a) (0.2 M) H_2O_2, pH = 6.5. and (0.001 g) NSC**1**, (b) (0.2 M) H_2O_2, PH = 6.5 and (0.001 g) TiO_2/NSC**1** composite.

linearly as $[H_2O_2]$ increases over the concentration range. The linearity of the plot and the calculated slope ($K_t = 5.57 \times 10^{-6}$ L mol^{-1} min^{-1}) exhibits a first-order relationship with hydrogen peroxide. The reaction rate increases directly with hydrogen peroxide concentration throughout this specific range. Under specified conditions, hydrogen peroxide functions as the primary limiting reactant, which directly controls the overall reaction rate. The results obtained from this study become fundamental for enhancing reaction performance in photocatalytic and advanced oxidation systems that utilize hydrogen peroxide as their primary oxidizing agent.

At low H_2O_2 concentrations, the kinetic deciding step is the generation of the $^{\bullet}OH$ radicals. As the starting H_2O_2 concentration increased to 0.50 M, the measured rate increased steadily (Fig. 7). An excess of H_2O_2 scavenging $^{\bullet}OH$ radicals causes the lower part of the curve, while an increase in the concentration of $^{\bullet}OH$ radicals generated *in situ* causes the rising section. More $^{\bullet}OH$ radicals were produced by higher H_2O_2 concentrations, and these radicals preferentially interacted with the excess H_2O_2 to form $HO_2^{\bullet}$, a less active per-hydroxyl radical.[91,92] This undesirable process competes with the dye chromophore's breakdown.[92] This behavior implies that there is a recommended H_2O_2 dose.

Another element that has a major impact on the MB dye's discoloration efficacy is pH. Standard quantities of the dye (2.2×10^{-4} M) and H_2O_2 (0.2 M), along with a set quantity of the composite catalyst (0.008 g), were used to examine the impact of pH on the reaction rate at pH values of 4–8, Fig. S11 and Table 3. The rate of deterioration under acidic conditions (pH = 4) is ($D\%$ = 94.36 for 5 minutes). The time increased to 18 minutes with $D\%$ = 98.125 and to 20 minutes with $D\%$ = 98.125 with pH = 5 and 5.5, respectively. The time steadily decreases from 12 to 8 minutes at higher pH values (6–8), with $D\%$ = 98.06 at 8 minutes, Table 3, Fig. S11 and 7. The initial reaction rate exhibits a remarkably fast increase as the pH level surpasses 6 and reaches its peak at 8. The data indicate that the photocatalytic process experiences major enhancements under alkaline conditions because of enhanced reactive oxygen species production and better catalyst surface activity. The relationship between pH and photocatalytic performance occurs because the

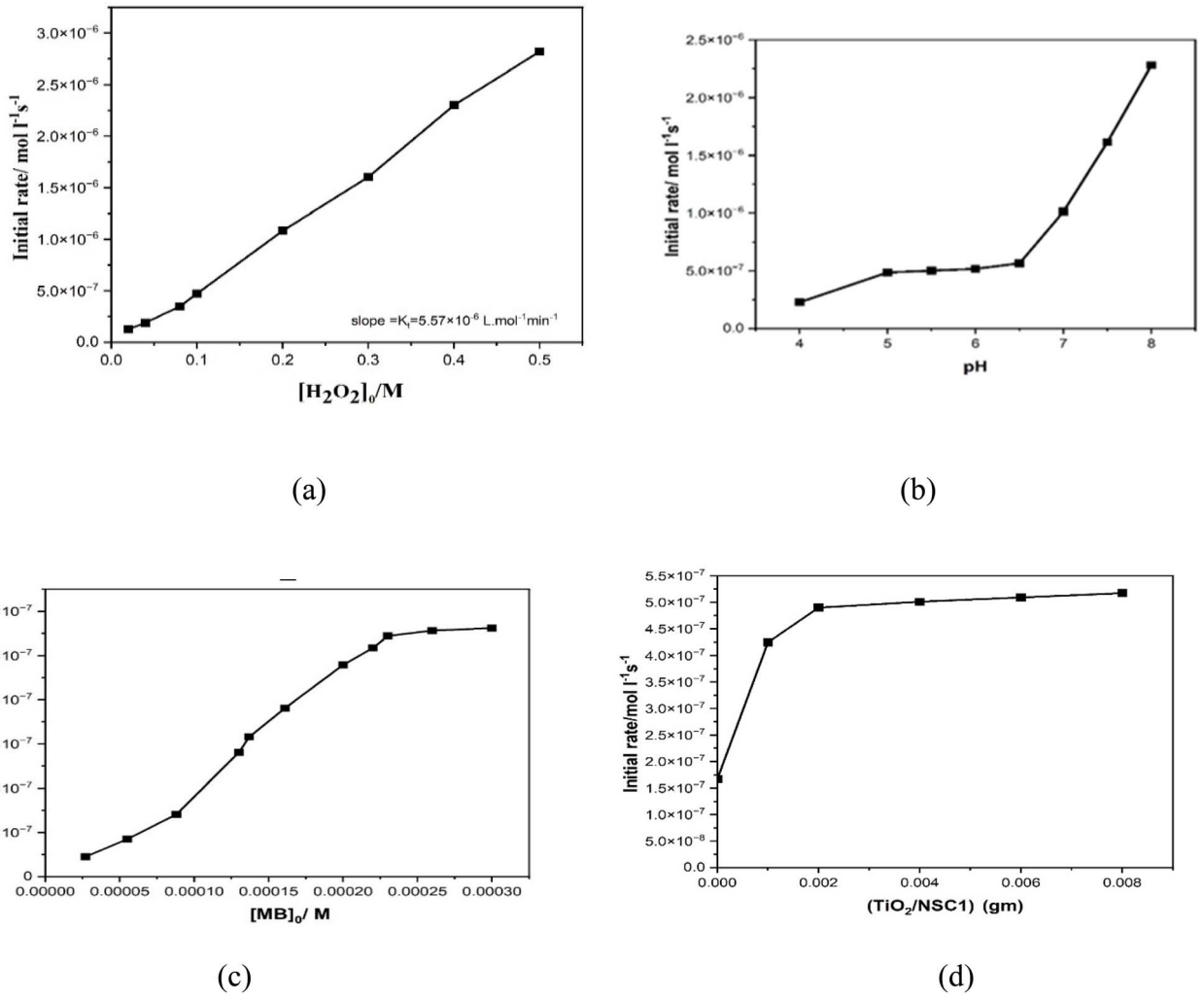

Fig. 7 Initial reaction rate dependence on (a) $[H_2O_2]_0$ concentration, (b) pH, (c) $[MB]_0$ concentration, and (d) the amount of the TiO_2/NSC1 composite. $[H_2O_2]$ = 0.2 M, pH = 6.5 and T = 30 °C.

Table 3 Catalytic degradation kinetics of MB dye utilizing the TiO_2/NSCP1 catalyst under different conditions

Parameter	k_{obs} (min^{-1})	Initial rate (mol L^{-1} s^{-1})	R^2	Time (min)	D (%)
[H_2O_2]/[M]					
0.02	0.01525	1.264×10^{-7}	0.5012	90	61.8
0.04	0.03909	1.9026×10^{-7}	0.8725	55	83.125
0.08	0.06416	3.481×10^{-7}	0.9007	40	95
0.1	0.23119	4.72×10^{-7}	0.9800	16	98.125
0.2	0.32455	1.083554×10^{-6}	0.9473	12	98.75
0.3	0.91913	3.647×10^{-7}	0.91	6	99.125
0.4	0.99708	2.303064×10^{-6}	0.9978	6	99.3
0.5	1.3074	2.81833×10^{-6}	0.99708	3	97.875
pH					
4	0.1354	2.081×10^{-7}	0.9807	16	95.12
5	0.23119	4.859×10^{-7}	0.9800	18	98.125
5.5	0.19579	5.019×10^{-7}	0.9700	20	98.125
6	0.35566	5.172×10^{-7}	0.8925	12	97.43
6.5	0.34433	5.652×10^{-7}	0.8783	8	96.06
7	0.64677	1.013×10^{-6}	1	9	97.25
7.5	0.44888	1.613×10^{-6}	0.9940	8	96.93
8	0.78942	2.27×10^{-6}	0.99905	5	98.06
[MB]/[M]					
5.5×10^{-5}	0.04	8.8×10^{-8}	0.98	42	80.48
8.2×10^{-5}	0.0459	1.41×10^{-7}	0.959	35	81.25
1.3×10^{-4}	0.145	2.81×10^{-7}	0.68	11	75.9
1.4×10^{-4}	0.264	3.16×10^{-7}	0.95	8	93.1
1.6×10^{-4}	0.308	3.81×10^{-7}	0.968	11	97.75
2×10^{-4}	0.175	4.79×10^{-7}	0.97	11	95.54
2.2×10^{-4}	0.324	5.17×10^{-7}	0.82	12	99.187
2.3×10^{-4}	0.184	5.43×10^{-7}	0.8	15	97.09
2.6×10^{-4}	0.14	5.5×10^{-7}	0.757	18	98.42
2.9×10^{-4}	0.117	5.61×10^{-7}	0.957	22	98.62
TiO_2/NSC1 (g)					
0.0	0.00282	1.66×10^{-7}	0.9654	600	47.14
0.001	0.17888	4.242×10^{-7}	0.988	24	98.93
0.002	0.24562	4.9×10^{-7}	0.98936	18	98.87
0.004	0.29083	5.01×10^{-7}	0.98807	15	98.75
0.006	0.2824	5.09×10^{-7}	0.96541	16	99.125
0.008	0.32455	5.172×10^{-7}	0.96635	12	99.18

catalyst surface charge and reactant speciation become heavily modified by the solution pH, which results in different efficiency levels for the degradation reaction efficiency (94.36–98.06%), Table 3. Although the $[MB]_0$ concentration was altered between (5.5×10^{-5} and 2.9×10^{-4}) mol L^{-1} under typical conditions, the impact of the initial concentration of MB dye on the reaction rate was investigated at pH = 6.5, Fig. 7. The reaction continues to follow first-order kinetics regarding the MB dye concentration within this concentration range. Table 3 shows that the initial rate increased progressively as the concentration of MB dye increased, but the degradation time changed substantially from 8 to 42 minutes, with the dye's degradation efficiency varying from 75.9 to 99.187%, Table 3.

Another important factor affecting the mineralization efficiency of MB dye is the effect of TiO_2/NSC**1** composite concentration. The concentration of the composite catalyst varies from 0.001 to 0.008 g, Fig. S12. The time of mineralization of MB started to decrease from 24 min to 12 min as the concentration of the catalyst increased to 0.008, with nearly the same degradation efficiency (98.75–99.125%), Table 3 and Fig. 7.

Given the normal conditions for BG dye degradation, it can be shown that the TiO_2/NSC**1** composite is more active than the catalyst NSC**1**, with $D\% = 99.33$ for the composite and $D\% = 99.0$ for NSC**1** after 20 and 42 minutes, respectively. Additionally, with ultrasonic radiation, the dye mineralizes in 6 minutes as opposed to 15 minutes under UV light (Fig. S13).

3.6. Recycling and analysis of the catalyst after catalytic reactions

After the experiment is finished, to investigate the feasibility of catalyst recycling, the catalyst is cleaned with double-distilled water, dried, and then subjected to another experiment. Under typical conditions, the composite catalyst TiO_2/NSC**1** continued to exhibit catalytic activity for four dye oxidation cycles, Fig. 8 and S14. Although the catalytic activity marginally declines and takes longer after the fourth cycle (first recycle $D\%$

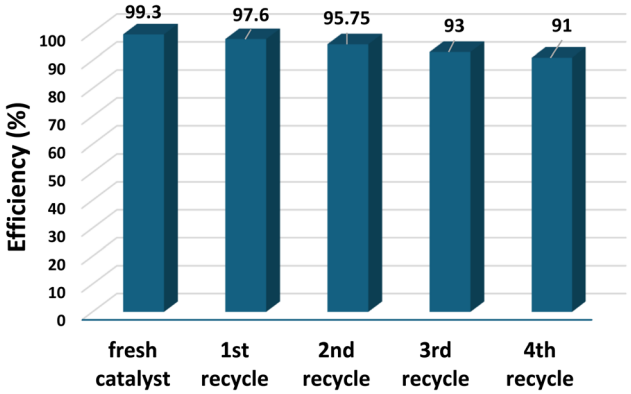

Fig. 8 Reusing the catalyst's ability to break down MB dye over TiO_2/NSC**1** many times.

= 97.6 within 18 min, 2nd cycle $D\%$ = 95.75 in 22 min, 3rd recycle $D\%$ = 93% within 26 min, 4th recycling $D\%$ = 91% in 27 min), after the third recycling, the deterioration time and efficiency remain constant as they would under normal conditions. When compared to the TiO_2/NSC**1** IR spectrum, the composite catalyst's IR spectrum after the degradation processes revealed no shift in the placement of the bands, and the catalyst was unaffected by the reaction medium, particularly since it was not oxidized by H_2O_2 and maintained its identity (Fig. S2 – IR present – *vide supra*).

The experimental XRBD patterns of TiO_2/NSC**1** prior to and following degradation were contrasted *via* the expected pattern of XRD of NSC**1** (Fig. 2-vide supra). The finished bulk powdered samples of **1** are structurally robust and stable, as shown by the agreement between the calculated XRD pattern of the NSCP**1** single crystals and the experimental XRBD patterns. The notable widening of the peaks suggests that the diameters of the particles are still in nanometers. These findings provide evidence that the composite catalyst's structure retains its structural identity following catalytic cycles.

3.7. Degradation products analyses

FT-IR and UV-spectra were used to track the products that were still in solution after MB and BG degradation by the TiO_2/NSC**1** catalyst, Fig. S15 and S16. The IR spectra of the dyes before degradation clearly show the characteristic C=N central ring stretching at 1600 cm^{-1}, C=C side ring stretching at 1482 cm^{-1}, multiple ring stretching at 1384 cm^{-1}, C_{Ar-N} (the connection between the nitrogen atom and the side aromatic ring) stretching at 1320 cm^{-1}, and $-CH_3$ stretching at 1240 and 1182 cm^{-1}.[93] The elimination of the characteristic bands after the catalytic reaction's conclusion showed that the MB and SG dyes had been destroyed by demethylation and the breakage of their side and central aromatic rings. The COO^-, SO_4^{2-} and $N(CH_3)_2$ stretching vibrations may be the cause of the appearance of 2 new, intense peaks at 1400–1350 and 1224 cm^{-1}, respectively,[93] indicating that the primary end products are the carboxylic acids CH_3COO^- and NO_3^- as well as SO_4^{2-} and SO_3^{2-} along with the prominent water bands at 3400 and 1620 cm^{-1}, which indicate that H_2O and CO_2 are the primary end products along with a few acids, Fig. S15 and S16 show the UV-Vis spectra and FTIR spectra of MB and BG dyes, both before and after degradation. The dye dimmer[94,95] and two bands in the UV range at 245 and 294 nm are responsible for the shoulder at 615 nm because of the MB dye dimmer's absorbance, which is not observed in the spectrum of BG. In contrast to the substituted benzene rings of BG and MB dyes, which have absorption bands in the UV region at 260–275 (^1L_a) and at 312–335 nm (^1L_b), the conjugation mechanism between the substituted aromatic rings causes absorbance at 625 and 668 nm. The absorbance of the dye dimmer has been identified as the cause of the little shoulder at 615 nm of MB. It was evident that the absorption peaks at 625 nm and 668 nm quickly disappeared. This showed that (BG) and (MB) degraded quickly, which is easier to accomplish when the TiO_2/NSC**1** catalyst is present. The visible bands of the (BG) and (MB) dyes were observed to gradually fade, while a few new bands began to appear at lower retention durations (Fig. S15 and S16). This demonstrates that the parent chemical was destroyed and that new compounds, with minor structural differences, like fewer methyl groups, were formed.

3.8. Identifying the primary active species involved in catalytic degradation

Ammonium oxalate (AO) and isopropanol (IPA) are utilized as scavengers. The generation of $^{\bullet}OH$ and h^+ active species on the catalyst TiO_2/NSC**1** surface was identified to ascertain whether active species are being produced in the dye/H_2O_2/catalyst processes to determine the generation of active species in the dye/H_2O_2/catalyst processes (Fig. 9) (Fig. S17 a and b). The degradation efficiency of MB dye was efficiently inhibited to 90.625% in 25 minutes by adding 2.5 M of IPA to the MB dye/H_2O_2/catalyst **1** system. Therefore, IPA quenches the $^{\bullet}OH$ radicals, suggesting that the rate at which $^{\bullet}OH$ radicals develop is a significant factor affecting catalytic activity. However, the addition of AO (D = 86.875% in 50 min) had a high impact on the catalytic degradation of MB dye, indicating that the $^{\bullet}OH$ radical has a stronger impact on the process of degradation than the active oxidation species h^+, Fig. 9 (Fig. S18). Additionally, the initial rate of methylene blue dye mineralization reduces as the concentration of isopropanol increases according to the effect of isopropanol concentration on this rate, suggesting that $^{\bullet}OH$ radicals are the primary active species, Fig. S18.

Therefore, the terephthalic acid disodium salt (NaTA) photoluminescence probing method can be used to specifically monitor the radicals of $^{\bullet}OH$, which, in catalytic and photocatalytic reactions, are the main active oxidation species. The luminous 2-hydroxy terephthalic acid (HTA) is produced when NaTA combines with $^{\bullet}OH$ radicals.[96] NaTA can thus be considered a selective and sensitive probe to detect the radicals of $^{\bullet}OH$ since it is unaffected by the presence of other reactive species, such as $O_2^{\bullet-}$, $HO_2^{\bullet-}$, and H_2O_2.[97,98] The fluorescence intensity of the H_2O_2/TiO_2/NSC**1**/NaTA system sharply increases to 940 in just seven minutes, demonstrating that the solution did, in fact,

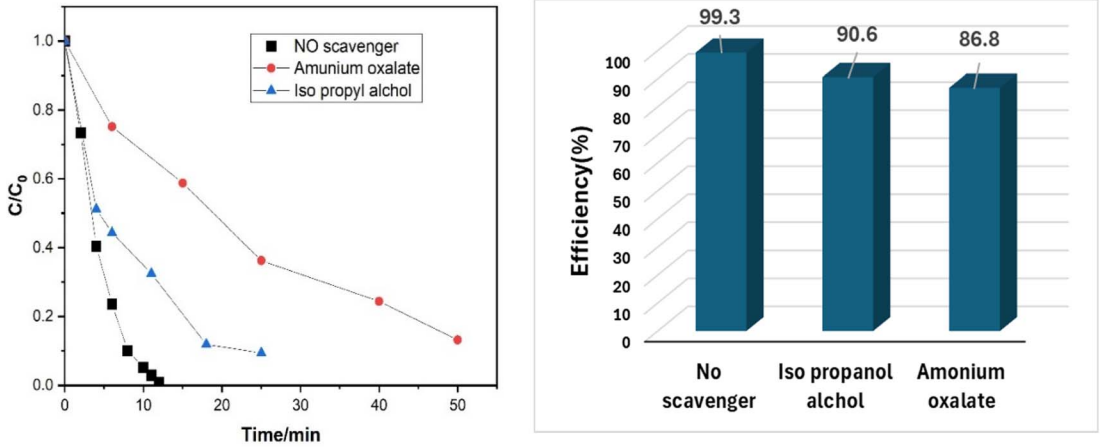

Fig. 9 Catalytic breakdown of MB dye over NSC**1** in isopropanol and ammonium oxalate scavenger solutions.

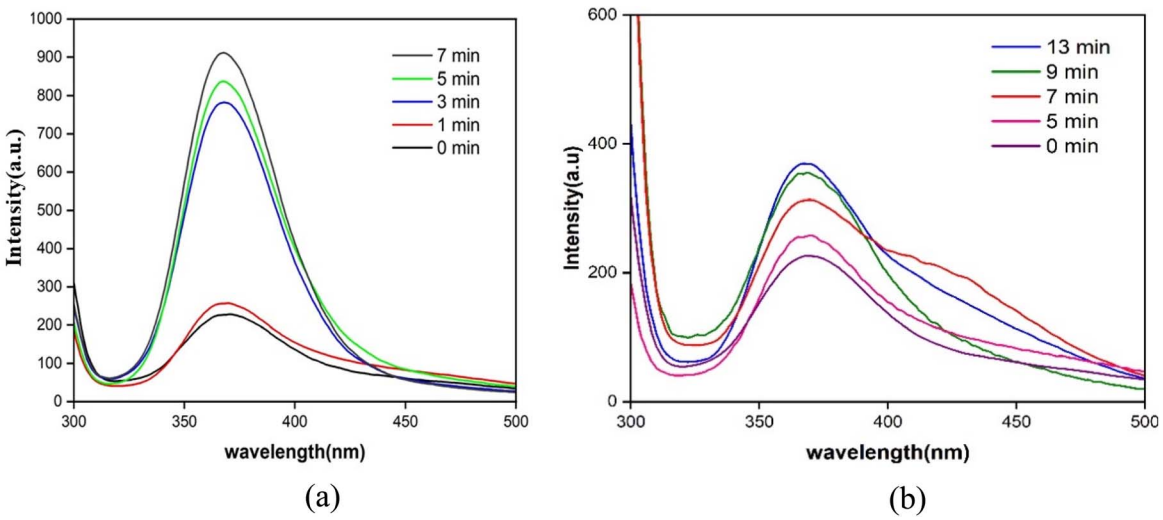

Fig. 10 Photoluminescence spectra of the (0.008) gm TiO_2/NSC**1** catalyst (0.001 M), NaTA, and H_2O_2 (0.2 M) at pH 6.5 as a function of time. In the absence of MB dye (a) and in the presence of MB dye (b).

create ˙OH radicals, Fig. 10. Nevertheless, the produced fluorescence dramatically dropped after the solution was mixed with MB dye and NaTA at the same time; the intensity increased to only 365 in 13 minutes, Fig. 10. In this instance, the decolorization observed during fluorescence measurement indicated that several of the ˙OH radicals had rapid interactions with the MB dye.

3.9. Mechanism of the reactions for both catalytic and photo-catalytic degradation

The redox characteristics of H_2O_2 have been proposed as a reaction mechanism based on experimental results and observations. These characteristics include a cyclic electron transfer process that is started by either moving an electron from H_2O_2 to the catalyst's oxidizing sites to create the $HO_2^{\cdot}$ radical or moving an electron from the catalyst's reducing sites to H_2O_2 to create ˙OH.[97,98] According to these findings, a mechanism involving the reaction of the catalyst under test with H_2O_2 to produce extremely aggressive oxidizing species, particularly ˙OH radicals, can be proposed. The degradation of products in this instance is the result of interactions between the radical species. It is possible to suggest a reaction mechanism that includes free radical species.

$$TiO_2/NSC\mathbf{1} + H_2O_2 \rightleftharpoons [TiO_2/NSC\mathbf{1}\text{–}H_2O_2] \quad (2)$$

Electron transfer set up complex

$$[TiO_2/NSC\mathbf{1}\text{–}H_2O_2] \rightleftharpoons TiO_2/NSC\mathbf{1} + {}^{\cdot}OH + {}^{-}OH \quad (3)$$

$$TiO_2/NSC\mathbf{1} + {}^{-}OH \rightarrow TiO_2/NSC\mathbf{1} + {}^{\cdot}OH \quad (4)$$

$$\text{Dye} + {}^{\cdot}OH \rightarrow \text{oxidation products} + H_2O + CO_2 \quad (5)$$

$${}^{\cdot}OH + \text{dye} \rightarrow H_2O + \text{dye} \quad (6)$$

The hydroxyl radical spreads the reaction by reacting with the organic color to produce additional radicals, which can then react in other ways.

$$\text{Dye} + H_2O_2 \rightarrow \text{dye–OH} + {}^{\bullet}OH \quad (7)$$

There are numerous other possible reactions, including the radical–radical reaction and the interaction of the $^{\bullet}OH$ radical with H_2O_2.

$$^{\bullet}OH + {}^{\bullet}OH \rightarrow H_2O_2 \quad (8)$$

The alternative is that the $HO_2^{\bullet}$ radical could be produced by an electron from H_2O_2 moving to the catalyst's oxidizing sites.

$$TiO_2/NSC\mathbf{1} + H_2O_2 \rightarrow HO_2^{\bullet} + TiO_2/NSC\mathbf{1}\text{–}H^+ \quad (9)$$

$$HO_2^{\bullet} + H_2O \rightarrow H_2O_2 + {}^{\bullet}OH \quad (10)$$

$$^{\bullet}OH + \text{dye} \rightarrow \text{oxidation products} + H_2O + CO_2 \quad (11)$$

Furthermore, under normal conditions, increasing the generation of $^{\bullet}OH$ radicals by UV or ultrasonic waves may improve the dye's degradation efficiency. The following equations show how H_2O_2 and UV light can be used to create $^{\bullet}OH$ radicals.

$$h\nu + H_2O_2 \rightarrow 2{}^{\bullet}OH \quad (12)$$

By forcing electrons from the valence band (VB) into the conduction band (CB), ultraviolet light can affect the catalyst.[99] Eqn (12) illustrates that the same number of positive holes (h^+) leave the VB because of electron transfer. $^{\bullet}OH$ radicals are created when h^+ oxidizes H_2O (eqn (18)) and e^- decreases O_2 (eqn (13)–(17)). H^+ and $O_2^{\bullet-}$ are the products of these reactions. $^{\bullet}OH$ radicals attack the dye molecules, reducing them to oxidation products CO_2 and H_2O (eqn (6) and (7)).

$$NSC\mathbf{1} + h\nu \rightarrow h_{VB}{}^+ + e_{CB}{}^- \quad (13)$$

$$e_{CB}{}^- + O_2 \rightarrow {}^{\bullet}O_2^- \quad (14)$$

$$^{\bullet}O_2^- + H^+ \rightarrow {}^{\bullet}OOH \quad (15)$$

$$2{}^{\bullet}OOH \rightarrow O_2 + H_2O_2 \quad (16)$$

$$H_2O_2 + h\nu \rightarrow 2{}^{\bullet}OH \quad (17)$$

$$h_{VB}{}^+ + H_2O \rightarrow {}^{\bullet}OH + H^+ \quad (18)$$

H_2O can divide using ultrasonic waves [)))] in accordance with eqn (19)–(22).

$$H_2O \overset{)))}{\rightarrow} {}^{\bullet}H + {}^{\bullet}OH \quad (19)$$

$$^{\bullet}OH + {}^{\bullet}OH \rightarrow H_2 + O_2 \quad (20)$$

$$^{\bullet}H + O_2 \rightarrow {}^{\bullet}OOH \quad (21)$$

Eqn (22)–(24) states that ultrasonic radiation promoted H_2O_2 breakdown in the reaction medium.[74]

$$H_2O_2 \overset{)))}{\rightarrow} 2{}^{\bullet}OH \quad (22)$$

$$e_{CB}{}^- + H_2O_2 \rightarrow {}^{\bullet}OH + OH^- \quad (23)$$

$$^{\bullet}O_2^- + H_2O_2 \rightarrow {}^{\bullet}OH + OH^- + O_2 \quad (24)$$

Finally, eqn (6) and (7) demonstrate that the investigated dyes are efficiently oxidized by $^{\bullet}OH$ radicals to yield degradation products.

However, more thorough tests are required to determine the true process, and these are now being investigated. Additionally, more studies should be conducted on NSC**1**'s and the composite promising catalytic activity for organic processes, where a *C*2-symmetric phen ligand and a copper(I) complex are included in their structures.[100]

3.10. Analysis of fluorescence and detection of metal ions and organic solvent molecules

As previously discussed, phen and CuCN are recognized as emissive chemicals in both solid and solvent states. Nevertheless, the development of the NSC**1** and TiO_2/NSC**1** composite makes it possible to tune the photophysical properties of CuCN and phen. The red shift of TiO_2/NSC**1**'s main band at 390–420 (ex = 280 nm) from the UV to the visible spectra is slightly greater than that of phen. Therefore, for certain metals and liquids, TiO_2/NSC**1**'s fluorescence characteristic can be used as a sensor. For additional research, the TiO_2/NSC**1** composite was suspended in several organic solvents to examine how solvent molecules affect fluorescence behavior.

To create suspensions by ultrasonography, 3 mg of TiO_2/NSC**1** was ground into a fine powder and then submerged in 10 mL of various widely used organic solvents, such as IPA, MeOH, EtOH, DMF, DMSO, nitrobenzene (NB), and MeCN. The fluorescence spectra of these suspensions in different solvents were then recorded. The kind of solvent determines the fluorescence intensity band, as shown in Fig. 11. This is most likely caused by the many ways in which solvent molecules interact with the composite, causing quenching efficacy.

IPA-related high intensity band, whereas NB shows a markedly quenching feature, Fig. 11. To assess the quantitative quenching efficiency of TiO_2/NSC**1**, NB doses ranging from 40 to 9×10^6 μM were gradually added to the composite suspension (3 mg) suspended in 3 mL of H_2O.[101,102] As the NB concentration steadily increased from 40 to 9×10^6 μM, the luminescence intensity of TiO_2/NSC**1** gradually reduced until it vanished completely (Fig. 12).

By utilizing the Stern–Volmer equation, which reads $I_0/I = 1 + K_{sv}[M]$, where [M] is the concentration of NB, K_{sv} is the quenching constant, and I_0 and I are the fluorescence intensities of the composite before and after adding NB, respectively. At low NB concentrations, the Stern–Volmer curve is linear (Fig. S19a). The K_{sv} was determined to be 25 850 M^{-1}, which is consistent with the coordination polymers previously described

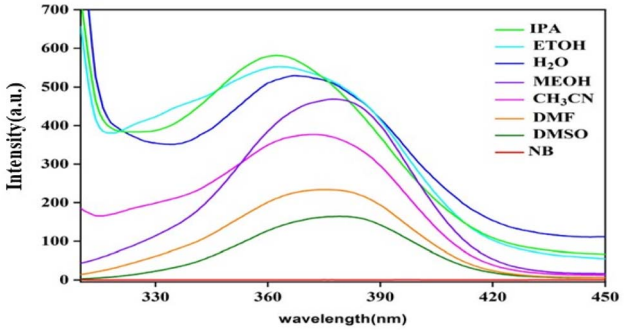

Fig. 11 TiO_2/NSC**1** nanocomposite luminosity spectra in various solvents.

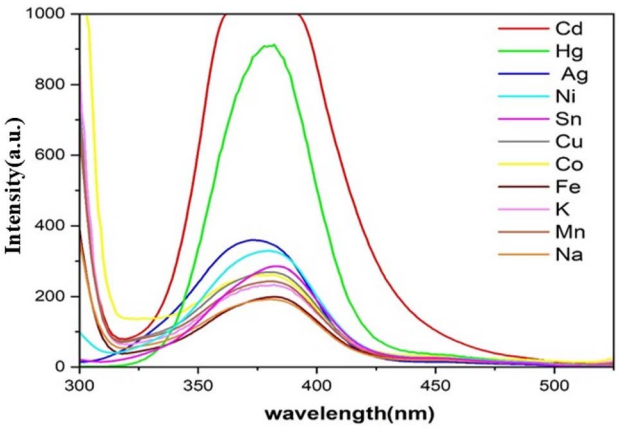

Fig. 13 Luminescence spectra of the TiO_2/NSC**1** nanocomposite with the addition of different metals.

for application in NB sensing.[103–105] The formula $QE = (I_0 - I)/I_0 \times 100\%$ was used to obtain the quenching efficiency (QE).[105] The maximum percentage of NB quenching against TiO_2/NSC**1** fluorescence was observed at a dose of 350 μM, where the QE was 96.8% (Fig. S19).[106]

The equation $LOD = 3\sigma/k$[107] was used to determine the limit of detection (LOD), where σ is the standard deviation for TiO_2/NSC**1** intensity without NB and k is the slope between luminescence intensity and concentration (Fig. S19). The LOD was determined to be 0.945 μM, which does not exceed the EPA's (U.S. Environmental Protection Agency) limit tolerance of 5.4 μM.[108] The excellent quenching effectiveness of 96.8% and the relatively low detection limit of 0.945 μM suggest that the TiO_2/NSC**1** composite is an effective luminous sensor for NB detection.

The photo-induced electron transfer mechanism was proposed as the basis for the quenching mechanisms of NB.[109] NB is electron-deficient and lies in the region between the SC1's valence band (VB) and conduction band (CB). Luminescence quenching occurs because of electron transport from the composite CB to NB during excitation. However, using the fluorescence resonance energy transfer (FRET) method, fluorescence quenching can occur when the π-conjugated phen ligand, which is employed to create TiO_2/NSC**1** composite, transfers its efficient energy to NB upon excitation.[110] Additionally, NB can create hydrogen bonds with the phen ligand and water molecules.[111]

We are advised to investigate the potential of TiO_2/NSC**1** composite as a sensor to identify different metal ions due to its exceptional luminescence capabilities in both solid state and various solvents. 3 mg of the composite was dissolved in water in addition to $M(NO_3)_n$ (1×10^{-3} mol L^{-1}) at the same concentrations, M = (Cd^{2+}, Hg^{+}, Na^{+}, Na^{+}, Ni^{2+}, Sn^{2+}, Cu^{2+}, Co^{2+}, Fe^{2+}, K^{+}, Mn^{2+}, and Ag^{+}) in order to conduct the sensing experiments. The equivalent fluorescence intensity was then evaluated at room temperature after the material was exposed to an ultrasonic treatment for ten minutes after excitation at 340 nm. The metal ions displayed varying fluorescence intensities with TiO_2/NSC**1**, as shown in Fig. 13. Na^{+} and Mn^{2+},

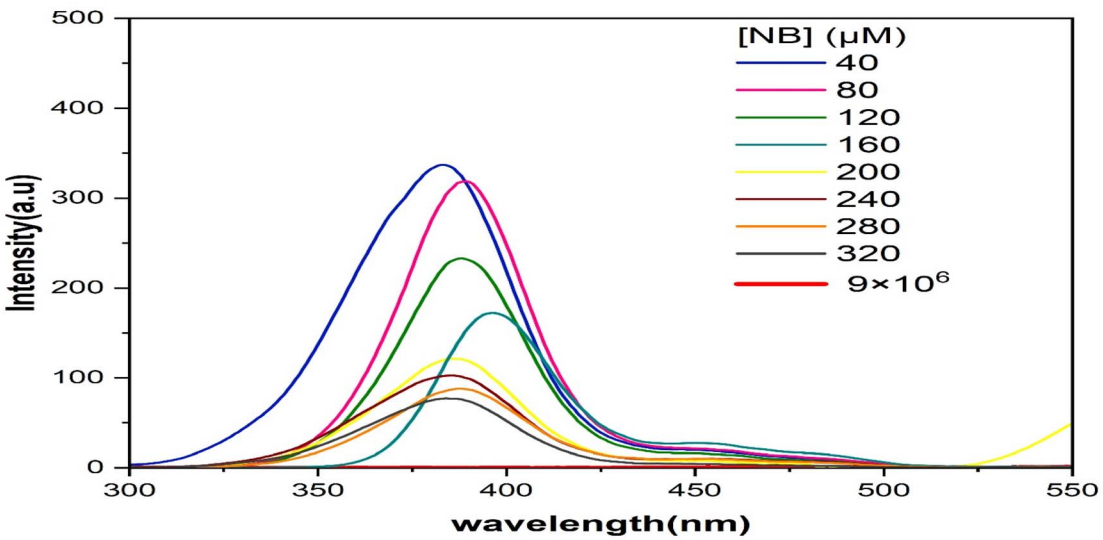

Fig. 12 Impact of [NB] addition on TiO_2/N nanocomposite emission spectra in H2O suspension.

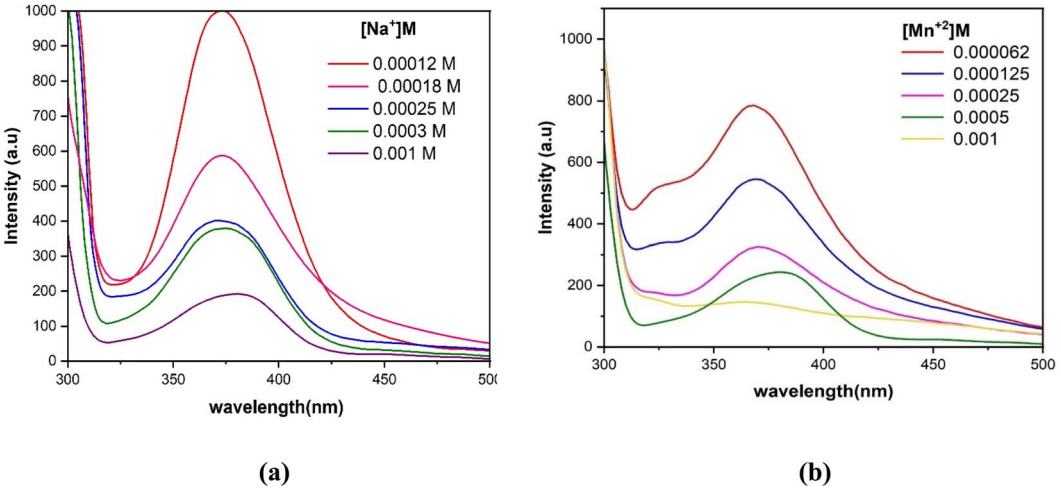

(a) (b)

Fig. 14 Luminescence spectra of the TiO_2/NSC**1** nanocomposite with the addition of different concentrations of Na^+ (a) and Mn^{2+} (b) ions.

however, demonstrated the strongest quenching effect. TiO_2/NSC**1** composite can therefore detect Na^+ and Mn^{2+} ions with excellent sensitivity and selectiveness.

The TiO_2/NSC**1** composite's emission spectra in H_2O in addition to different concentrations of Na^+ and Mn^{2+} ions were examined at room temperature to conduct a more thorough detection analysis of the sensitivity of the composite towards these ions, as depicted in Fig. 14. With each additional increase in Na^+ or Mn^{2+} ion concentration, which ranged from 1.2×10^{-4} to 1×10^{-3} M or 0.62×10^{-4} to 1×10^{-3} M, respectively, the emission intensity of the TiO_2/NSC**1** composite dispersed in H_2O steadily decreased. At a concentration of 1×10^{-3} M for Na^+ and Mn^{2+} ions, complete quenching takes place (Fig. S20 and S21a–c).

The Stern–Volmer equation revealed that the *S–V* curve was almost linear at low concentrations of Na^+ and Mn^{2+} ions and departed from linearity at increasing values (Fig. S20 and S21a–c). Na^+ and Mn^{2+} ions were found to have quenching constants (K_{sv}) of 2878.5 and 4303.8, respectively. These values correspond to coordination polymers that have been previously reported to be employed as Na^+ and Mn^{2+} ion sensors.

According to the prior relation, Fig. S20(c) and S21(c), the quenching efficiency (QP) was computed and found to be 74.25% for Na^+ at 10^{-3} M and 83.1% for Mn^{2+} at 3×10^{-3} M. These results show that TiO_2/NSC**1** has a high quenching percentage against Na^+ and Mn^{2+} ions. The LOD values for Na^+ and Mn^{2+} were determined to be 1.13 M and 5.71 M, respectively (Fig. S20 and S21(b)).

Therefore, TiO_2/NSC**1**'s low detection limits and high quenching efficiencies of 74.25% and 83.1% demonstrate that it is a useful luminous sensor for the detection of Na^+ and Mn^{2+} ions. The quenching mechanism caused by Na^+ and Mn^{2+} ions can be inferred from the overlap of the emission band of TiO_2/NSC**1** with the electronic transition band of Na^+ or Mn^{2+} ions, which, in accordance with the fluorescence resonance energy transfer (FRET) mechanism, induces fluorescence quenching. The quenching process is also brought about by interactions between Lewis acidic metal cations and the TiO_2/NSC**1** composite.[112,113]

4. Conclusion

Single crystals of $[Cu(CN)(phen)_2[Cu(CN)_2(phen)](H_2O)_5]$ (NSC**1**) are produced by employing ultrasonic waves. The structure contains the Cu^I complex, which coordinates to two phen units *via* nitrogen atoms and one cyanide group adopting the (TBPY-5) geometry, and the Cu^{II} complex, which coordinates to one phen molecule and two cyanide groups to form the T-4 geometry

NSC**1**/TiO_2 composite and NSC**1** can be considered efficient heterogeneous catalysts for the elimination of organic dyes in aqueous solutions with H_2O_2 under UV-radiation or ultrasonic waves. However, the nano composite exhibits better catalytic performance than NSC**1** and TiO_2 separately. This method is simple and inexpensive and does not involve any stringent reaction conditions. The main active species are hydroxyl radicals according to scavengers and (NaTA) photoluminescence probing technology. Comparing the data of the composite with those in the literature, Table S4 supports the excellent activity of the composite compared to those reported in the literature.[114–130]

The TiO_2/NSC**1** nanocomposite's photoluminescence property functions as an effective, selective luminous sensor supported by data, which show that the nanocomposite has a high quenching efficiency for nitrobenzene, Na^+, and Mn^{2+} ions, as well as a good limit of detection. Additionally, the selective sensing capabilities of the TiO_2/NSC**1** composite allow for the independent quantitative determination of both Na^+ and Mn^{2+} ions.

Conflicts of interest

The authors declare no conflict of interest.

Data availability

The data that support the findings of this study are available from the corresponding author upon reasonable request.

Supplementary information is available. See DOI: https://doi.org/10.1039/d5ra06817g.

References

1 H. Wu, Y. Wang, L. Đorđević, P. Kundu, S. Bhunia, A. X.-Y. Chen, L. Feng, D. Shen, W. Liu, L. Zhang, B. Song, G. Wu, B.-T. Liu, M. Y. Yang, Y. Yang, C. L. Stern, S. I. Stupp, W. A. Goddard, W. Hu and J. F. Stoddart, Dynamic Supramolecular Snub Cubes, *Nature*, 2025, **637**(8045), 347–353.

2 H. Lee, H. Park, D. Y. Ryu and W.-D. Jang, Porphyrin-Based Supramolecular Polymers, *Chem. Soc. Rev.*, 2023, **52**(5), 1947–1974.

3 X. Xiao, H. Chen, X. Dong, J. Zhang, J. Zhang, H. Zhang, D. Wang and W. Tian, Controllable construction of an ordered three-dimensional supramolecular polymer with selective guest adsorption ability, *Mater. Chem. Front.*, 2022, **6**(21), 3261–3278.

4 H. R. Marsden and A. Kros, Self-assembly of coiled coils in synthetic biology: inspiration and progress, *Angew. Chem., Int. Ed.*, 2010, **49**, 2988.

5 C. Redshaw, Utilizing the Metal Coordination and Supramolecular Chemistry of Macrocyclic Ligands to Tackle Medicinal Issues, *Coord. Chem. Rev.*, 2025, **523**, 216147–216181.

6 B. L. Vinay, C. S. Karthik, M. K. Hema, J. R. Rajabathar, A. H. U. Kumar, B. N. Ramakrishna and N. K. Lokanath, Non-Covalent Interactions Orchestrated Distinct Molecular Arrangements along Different Axes within the Novel Mixed Ligand Thorium Metal Complex: Experimental and Theoretical Insights, *J. Mol. Struct.*, 2024, **1303**, 137486–13799.

7 Y. Jin, B. Ramadoss, S. Asako and L. Ilies, Noncovalent Interaction with a Spirobipyridine Ligand Enables Efficient Iridium-Catalyzed C-H Activation, *Nat. Commun.*, 2024, **15**(1), 2886–2894.

8 K. Shi, X. Lv, J. Liu, Y. Lin and J. Li, Mechanically Active Supramolecular Systems, *Small Sci.*, 2024, **4**(5), 2300300–2300308.

9 A. Winter and U. S. Schubert, Synthesis and characterization of metallo-supramolecular polymers, *Chem. Soc. Rev.*, 2016, **45**(19), 5311–5368.

10 K. Buaksuntear, K. Panmanee, K. Wongphul, P. Lim-arun, S. Jansinak, D. U. Shah and W. Smitthipong, Enhancing Mechanical Properties and Stabilising the Structure of Epoxide Natural Rubber Using Non-Covalent Interactions: Metal-Ligand Coordination and Hydrogen Bonding, *Polymer*, 2024, **291**, 126626–126640.

11 T. Park and S. C. Zimmerman, Formation of a Miscible Supramolecular Polymer Blend through Self-Assembly Mediated by a Quadruply Hydrogen-Bonded Heterocomplex, *J. Am. Chem. Soc.*, 2006, **128**(35), 11582.

12 T. Ogoshi and T. Yamagishi, Pillar [5]- and pillar [6] arene-based supramolecular assemblies built by using their cavity-size-dependent host-guest interactions, *Chem. Commun.*, 2014, **50**(37), 4776.

13 H. Li, C. Wang, X. Bai, X. Wang, B. Sun, D. Li, L. Zhao, R. Zong and D. Hao, In-plane polarization induced by the hydrogen bonding and π-π stacking of functionalized PDI supramolecules for the efficient photocatalytic degradation of organic pollutants, *Mater. Chem. Front.*, 2020, **4**(9), 2673.

14 H. Y. Lee, S. H. Park, J. H. Kim and M. S. Kim, Temperature-responsive hydrogels via the electrostatic interaction of amphiphilic deblock copolymers with pendant-ion groups, *Polym. Chem.*, 2017, **8**(43), 6606.

15 C. Rest, R. Kandanelli and G. Fernández, Strategies to create hierarchical self-assembled structures via cooperative non-covalent interactions, *Chem. Soc. Rev.*, 2015, **44**(8), 2543.

16 W. A. Wani, A. Hussain, S. Amir, M. F. Alajmi, A. H. Malik, A. Khursheed and W. A. Khanday, Emergence of Macrocyclic Metal Complexes as Anticancer Agents, in *Anticancer Potential of Macrocyclic Metal Complexes; ACS Symposium Series 1492*, American Chemical Society, Washington, DC, 2025, ch. 1, pp. 1–12.

17 L. I. Matienko, E. M. Mil, A. A. Albantova and A. N. Goloshchapov, Selective Catalysis by Complexes Including Ni and Redox-Inactive Alkali Metals (Li, Na, or K) in Oxidation Processes: The Role of Hydrogen Bonds and Supramolecular Structures, *Int. J. Mol. Sci.*, 2025, **26**(3), 1166.

18 D. B. Amabilino, D. K. Smith and J. W. Steed, Supramolecular Materials, *Chem. Soc. Rev.*, 2017, **46**(9), 2404.

19 J. Zhou, L. Rao, G. Yu, T. R. Cook, X. hen and F. Huang, Supramolecular Cancer Nanotheranostics, *Chem. Soc. Rev.*, 2021, **50**(4), 2839.

20 B. Li, P.-F. Cao, T. Saito and A. P. Sokolov, Intrinsically Self-Healing Polymers: From Mechanistic Insight to Current Challenges, *Chem. Rev.*, 2023, **123**(2), 701.

21 K. Nakano, H. Sato, M. Muraoka and M. Shizuma, Photo- and thermo-responsive supramolecular polymer networks via in situ polymerization using homoternary macrocyclic host with coumarin monomers in water, *Polym. Chem.*, 2022, **13**(4), 5820–5828.

22 K. Wu, N. Lam, D. A. Strassfeld, Z. Fan, J. X. Qiao, T. Liu, D. Stamos and J. Yu, Palladium (II)-Catalyzed C−H Activation with Bifunctional Ligands: From Curiosity to Industrialization, *Angew. Chem., Int. Ed.*, 2024, **63**(19), e202400509.

23 X. Y. Zhu, X. N. Yang, Y. Luo, C. Redshaw, M. Liu, Z. Tao and X. Xiao, Construction of a Supramolecular Fluorescence Sensor from Water-soluble Pillar [5] arene and 1-Naphthol for Recognition of Metal Ions, *ChemistrySelect*, 2021, **6**(46), 12942.

24 S. Maity, V. K. Deb, S. Mondal, A. Chakraborty, K. Pramanick and S. Adhikari, Leveraging Supramolecular

Systems in Biomedical Breakthroughs, *BioFactors*, 2025, **51**(1), e70005.

25 X. Ji, Y. Yao, J. Li, X. Yan and F. Huang, A Supramolecular Cross-Linked Conjugated Polymer Network for Multiple Fluorescent Sensing, *J. Am. Chem. Soc.*, 2012, **135**(1), 74.

26 X.-M. Chen, X. Chen, X.-F. Hou, S. Zhang, D. Chen and Q. Li, Self-assembled supramolecular artificial light-harvesting nano systems: construction, modulation, and applications, *Nanoscale Adv.*, 2023, **5**(7), 1830.

27 Y. Wang, D. Wang, J. Wang, C. Wang, J. Wang, Y. Ding and Y. Yao, Pillar [5] arene-derived covalent organic materials with pre-encoded molecular recognition for targeted and synergistic cancer photo- and chemotherapy, *Chem. Commun.*, 2022, **58**(11), 1689.

28 X. Yan, Y. Huang, M. Cen, J. Wang, J. Shi, B. Lu, Y. Wang and Y. Yao, Pillar[6]arene-ased supramolecular polymeric materials constructed via electrostatic interactions for rapid and efficient organic dye removal from water, *Nanoscale Adv.*, 2021, **3**(7), 1906.

29 L. Liu, Y. Hu, S. Huang, Y. Jin, J. Cui, W. Gong and W. Zhang, A pillar [5] arene-based covalent organic framework with pre-encoded selective host–guest recognition, *Chem. Sci.*, 2021, **12**(40), 13316.

30 Z. Li and Y.-W. Yang, Macrocycle-Based Porous Organic Polymers for Separation, Sensing, and Catalysis, *Adv. Mater.*, 2022, **34**(6), 2107401.

31 Z.-Q. Wang, X. Wang and Y.-W. Yang, Pillararene-Based Supramolecular Polymers for Adsorption and Separation, *Adv. Mater.*, 2023, **36**(4), e2301721.

32 X. Lv, D. Xia, Y. Cheng, y. Liu, J. Zhang, X. Wei and P. Wang, Supramolecular hyperbranched polymer gels based on pillar[5]arene and their applications in removal of micropollutants from water, *Inorg. Chem. Front.*, 2022, **9**(23), 6248.

33 H. R. Marsden and A. Kros, Self-assembly of coiled coils in synthetic biology: inspiration and progress, *Angew. Chem., Int. Ed.*, 2010, **49**, 2988.

34 D. Xia, P. Wang, X. Ji, N. M. Khashab, J. L. Sessler and F. Huang, Functional Supramolecular Polymeric Networks: The Marriage of Covalent Polymers and Macrocycle-Based Host-Guest Interactions, *Chem. Rev.*, 2020, **120**(13), 6070.

35 N. Thanvisitthpon, K. Kallawicha and H. J. Chao, Effects of Urbanization and Industrialization on Air Quality, in *Health and Environmental Effects of Ambient Air Pollution: Air Pollution, Human Health, and the Environment*, 2024, vol. 1, ch. 10, pp. 231–255.

36 B. Bera, S. Chinta, D. A. Mahajan, A. Sailaja and R. Mahajan, Urbanization and Its Impact on Environmental Sustainability: A Comprehensive Review, *J. Harbin Eng. Univ.*, 2023, **44**(8), 1310.

37 V. Saxena, Water Quality, Air Pollution, and Climate Change: Investigating the Environmental Impacts of Industrialization and Urbanization, *Water, Air, Soil Pollut.*, 2025, **236**(2), 73.

38 M. L. Qureshi, A. M. Rasli, U. Awan, J. Ma, G. Ali, A. Faridullah, A. Alam, F. Sajjad and K. Zaman, Environment and Air Pollution: Health Services Bequeath to Grotesque Menace, *Environ. Sci. Pollut. Res.*, 2015, **22**(5), 3467.

39 B. Sahu and J. C. Poler, Removal and Degradation of Dyes from Textile Industry Wastewater: Benchmarking Recent Advancements, Toxicity Assessment and Cost Analysis of Treatment Processes, *J. Environ. Chem. Eng.*, 2024, **12**(5), 113754.

40 P. Dutta, M. R. Rabbi, M. A. Sufian and S. Mahjebin, Effects of Textile Dyeing Effluent on the Environment and Its Treatment: A Review, *Eng. Appl. Sci. Lett.*, 2022, **5**(1), 1–17.

41 T. Akter, A. T. Protity, M. Shaha, M. A. Mamun and A. Hashem, The Impact of Textile Dyes on the Environment, in *Nanohybrid Materials for Treatment of Textiles Dyes*, 2023, ch. 1, p. 401.

42 D. G. Barceloux and D. Barceloux, Manganese, *Clin. Toxicol.*, 1999, **37**(2), 293.

43 (*a*) B. Hernroth, A.-S. Krång and S. Baden, Bacteriostatic suppression in Norway lobster (Nephrops norvegicus) exposed to manganese or hypoxia under pressure of ocean acidification, *Aquat. Toxicol.*, 2015, **159**, 217; (*b*) N. A. Metheny and M. M. Krieger, Salt Toxicity: A Systematic Review and Case Reports, *J. Emerg. Nurs.*, 2020, **46**(4), 428.

44 S. V. Feigin, D. O. Wiebers, G. Lueddeke, S. Morand, K. Lee, A. Knight, M. Brainin, V. L. Feigin, A. Whitfort, J. Marcum, T. K. Shackelford, L. E. Skerratt and A. S. Winkler, Proposed Solutions to Anthropogenic Climate Change: A Systematic Literature Review and a New Way Forward, *Heliyon*, 2023, **9**(10), e20544.

45 K. Yue, X. Zhang, S. Jiang, J. Chen, Y. Yang, E. Bi and Y. Wang, Recent Advances in Strategies to Modify MIL-125(Ti) and Its Environmental Applications, *J. Mol. Liq.*, 2021, **335**, 116108.

46 N. H. Abbas, R. Rasuli and P. N. Panahi, Decorated Titanium Oxide with Ag Nanoparticles as an Efficient Photocatalyst under Visible Light: A Novel Synthesis Approach, *Sci. Rep.*, 2025, **15**(1), 8207.

47 K. Nagaraj, S. Radha, C. G. Deepa, K. Raja, V. Umapathy, N. P. Badgujar, N. M. Parekh, T. Manimegalai, L. A. Devi and C. Uthra, Photocatalytic advancements and applications of titanium dioxide (TiO_2): Progress in biomedical, environmental, and energy sustainability, *Next Research*, 2025, **2**(1), 100180.

48 M. S. Sharifiyan, A. Fattah-alhosseini and M. Karbasi, Optimizing the Hydrothermal Post-Treatment Process for a TiO_2/WO_3 Hybrid Coating to Enhance the Photocatalytic Degradation of Methylene Blue under Visible Light, *Ceram. Int.*, 2023, **49**(22), 35175.

49 A. Fattah-alhosseini, M. Karbasi and H. A. Bahramian, Thorough Investigation of the Utilization of Metal-Organic Framework (MOF) Coated Titanium Dioxide in Photocatalytic Applications: A Review, *Appl. Surf. Sci. Adv.*, 2023, **18**, 100504.

50 A. Khlyustova, N. Sirotkin, T. Kusova, A. Kraev, V. Titov and A. Agafonov, Doped TiO_2: The Effect of Doping Elements on Photocatalytic Activity, *Mater. Adv.*, 2020, **1**(5), 1193.

51 Y. Yalçın, M. Kılıç and Z. Çınar, The Role of Non-Metal Doping in TiO_2 Photocatalysis, *J. Adv. Oxid. Technol.*, 2010, **13**(3), 281.

52 S. Goulart, L. J. J. Nieves, A. G. Dal Bó and A. M. Bernardin, Sensitization of TiO_2 Nanoparticles with Natural Dyes Extracts for Photocatalytic Activity under Visible Light, *Dyes Pigm.*, 2020, **182**, 108654.

53 R. Hosseini, A. Fattah-alhosseini, M. Karbasi and S. Giannakis, Tailoring Surface Defects in Plasma Electrolytic Oxidation (PEO) Treated 2-D Black TiO_2: Post-Treatment Role, and Intensification by Peroxymonosulfate Activation in Visible Light-Driven Photocatalysis, *Appl. Catal., B*, 2024, **340**, 123197.

54 H. Bahramian, A. Fattah-alhosseini, M. Karbasi, E. Nikoomanzari and S. Giannakis, Synergy of Cu^{2+}-$Cu(OH)_2$-CuO with TiO_2 Coatings, Fabricated via Plasma Electrolytic Oxidation: Insights into the Multifaceted Mechanism Governing Visible Light-Driven Photodegradation of Tetracycline, *Chem. Eng. J.*, 2023, **476**, 146588.

55 W. A. El Rouby, M. Antuch, S. M. You and P. Millet, Surface Sensitization of TiO_2 Nanorod Mats by Electrodeposition of ZIF-67 for Water Photo-Oxidation, *Electrochim. Acta*, 2020, **339**, 135882.

56 Q. Jiang, Y. Xiao, A. N. Hong, Z. Gao, Y. Shen, Q. Fan, P. Feng and W. Zhong, Bimetallic Metal-Organic Framework Fe/Co-MIL-88(NH_2) Exhibiting High Peroxidase-Like Activity and Its Application in Detection of Extracellular Vesicles, *ACS Appl. Mater. Interfaces*, 2022, **14**(37), 41800.

57 H. Lozano, S. Devis, J. Aliaga, M. Alegría, H. Guzmán, R. Villarroel, E. Benavente and G. González, Two-Dimensional Titanium Dioxide-Surfactant Photoactive Supramolecular Networks: Synthesis, Properties, and Applications for the Conversion of Light Energy, *Int. J. Mol. Sci.*, 2022, **23**(7), 4006.

58 C. P. A. Crake, K. C. Christoforidis, A. Gregg, B. Moss, A. Kafizas and C. Petit, The Effect of Materials Architecture in TiO_2/MOF Composites on CO_2 Photoreduction and Charge Transfer, *Small*, 2019, **15**(11), 1805473.

59 W. Xie, G. Liu, Y. Liu, Y. Bai, Y. Liao, T. Li, C. Wang, S. Chang and J. Hu, Multidimensional TiO_2 Photocatalysts for the Degradation of Organic Dyes in Wastewater Treatment, *J. Porous Mater.*, 2024, **31**(5), 1655.

60 L. Shen, S. Pang, M. Zhong, Y. Sun, A. Qayum, Y. Liu, A. Rashid, B. Xu, Q. Liang, H. Ma and X. Ren, A Comprehensive Review of Ultrasonic Assisted Extraction (UAE) for Bioactive Components: Principles, Advantages, Equipment, and Combined Technologies, *Ultrason. Sonochem.*, 2023, **101**, 106646.

61 W. I. Liu, O. Malekahmadi, S. A. Bagherzadeh, M. Ghashang, A. Karimipour, S. Hasani, I. Tlili and M. Goodarzi, A Novel Comprehensive Experimental Study Concerned Graphene Oxide Nanoparticles Dispersed in Water: Synthesise, Characterisation, Thermal Conductivity Measurement and Present a New Approach of RLSF Neural Network, *Int. Commun. Heat Mass Transfer*, 2019, **109**, 104333.

62 H. Karami, S. Pourafshary Zare, M. Shanbedi, H. Eshghi, A. Dashtbozorg, A. Akbari, E. Mohammadian, M. Heidari, A. Z. Sahin and A. Z. Teng, The Thermophysical Properties and the Stability of Nanofluids Containing Carboxyl-Functionalized Graphene Nano-Platelets and Multi-Walled Carbon Nanotubes, *Int. Commun. Heat Mass Transfer*, 2019, **108**, 104302.

63 I. M. Mahbubul, R. Saidur and M. A. Amalina, Influence of Ultrasonication Duration on Rheological Properties of Nanofluid: An Experimental Study with Alumina-Water Nanofluid, *Int. Commun. Heat Mass Transfer*, 2016, **76**, 33.

64 M. Noroozi, S. Radiman and A. Zakaria, Influence of Sonication on the Stability and Thermal Properties of Al_2O_3 Nanofluids, *J. Nanomater.*, 2014, (1), 612417.

65 M. Leena and S. Srinivasan, Synthesis and Ultrasonic Investigations of Titanium Oxide Nanofluids, *J. Mol. Liq.*, 2015, **206**, 103.

66 S. E. H. Etaiw, S. A. Amer and M. M. El-Bendary, A Mixed Valence Copper Cyanide 3D-supramolecular Coordination Polymer Containing 1,10-Phenathorline Ligand as a Potential Antitumor Agent, Effective Catalyst and Luminescent Material, *J. Inorg. Organomet. Polym.*, 2011, **21**, 662.

67 S. E. H. Etaiw and S. N. Abdou, New Organotin Supramolecular Complexes Based on Copper Cyanide and Auxiliary N-Donor Ligands as Potent Inhibitors of Cancer Cell Lines: In Vitro and Antioxidant Experiments, *Appl. Organomet. Chem.*, 2018, **32**(2), e4053.

68 H. Masuda, K. Machida, M. Munakata, S. Kitagawa and H. Shimono, Synthesis and structural study of (2, 2′-bipyridine)perchlorato(styrene)-copper(I), *J. Chem. Soc., Dalton Trans.*, 1988, **7**, 1907.

69 L. Stamp and T. Dieck, Copper (I) complexes with unsaturated nitrogen ligands. Part III. Copper (I) diazadiene complexes with carbon monoxide, olefins and acetylenes, *Chim. Acta*, 1987, **129**, 107.

70 T. Pintauer, Synthesis, Characterization, and the Role of Counterion in Stabilizing Trigonal Pyramidal Copper(I)/2, 2′-Bipyridine Complexes Containing Electron-Poor Methyl Acrylate, *J. Organomet. Chem.*, 2006, **691**(18), 3948.

71 T. E. Kokina, L. A. Glinskaya, D. A. Piryazev, A. Y. Baranov, A. M. Agafontsev, Y. A. Eremina, E. V. Vorontsova, A. S. Bogomyakov, D. Y. Naumov, A. V. Tkachev and S. V. Larionova, Synthesis and Structures of CuI, II Complexes with a 2, 2′-Bipyridine Derivative Bearing a (+)-3-Carene Moiety, *Russ. Chem. Bull.*, 2018, **67**(7), 1251.

72 R. H. Holm, P. Kennepohl and E. I. Solomon, Structural and Functional Aspects of Metal Sites in Biology, *Chem. Rev.*, 1996, **96**(7), 2239.

73 N. Kitajima, T. Katayama, K. Fujisawa, Y. Iwata and Y. Morooka, Synthesis, molecular structure, and reactivity of (alkylperoxo) copper (II) complex Inorg, *Chem. Commun.*, 1993, **115**(17), 7872.

74 I. Gumus, C. Ozer, D. Vanderveer and H. Arslan, Crystal Structure of cis-Copper(II) Complex with N-(Di-n-

propylcarbamothioyl) cyclohexane carboxamide Ligand, *Eur. J. Chem.*, 2016, **7**(4), 416.

75 L. Gutierrez, G. Alzuet, J. Borrás, M. Liu-González, F. Sanz and A. Castiñeiras, Influence of tetrahedral distortion of CuN 4 complexes on methylpyridyl) benzenesulfonylamidate) spectroscopic properties. Synthesis, characterization and crystal structures of [Cu(N-(2-2], [Cu(N-(2-methylpyridyl) toluenesulfonylamidate)2] and [Cu(N-(2-methylpyridyl) naphthalenesulfonylamidate)2] compounds, *Polyhedron*, 2001, **20**(7), 703.

76 X. C. Huang, S.-L. Zheng, J.-P. Zhang and X.-M. Chen, Synthesis, Structure and Photoluminescent Studies of a Novel Supramolecular [Ag(phen)(CN)]·(phen) Complex, *Eur. J. Inorg. Chem.*, 2004, (5), 1050.

77 A. Spalletti, G. Cruciani and U. Mazzucato, Conformational Equilibria in EE-2, 6-Di[2-(furan-2-yl) vinyl] pyridine Controlled by Intramolecular Hydrogen-Type Bonds, *J. Mol. Struct.*, 2002, **612**(2), 339.

78 H. H. Jaffé and M. Orchin, *Theory and Applications of Ultraviolet Spectroscopy*, 5th edn, Wiley, New York, 1970.

79 N. Armaroli, L. De Cola, V. Balzani, J.-P. Sauvage, C. O. Dietrich-Buchecker and J.-M. Kern, Absorption and luminescence properties of 1, 10-phenanthroline, 2, 9-diphenyl-1, 10-phenanthroline, 2, 9-dianisyl-1, 10-phenanthroline and their protonated forms in dichloromethane solution, *J. Chem. Soc., Faraday Trans.*, 1992, **88**(4), 553.

80 P. G. Sammes and G. I. Yahioglu, 10-Phenanthroline: a versatile ligand, *Chem. Soc. Rev.*, 1994, **23**(5), 327.

81 B. N. Bandyopadhyay and A. Harriman, Photoreduction of 1, 10-phenanthroline, *J. Chem. Soc., Faraday Trans. 1*, 1977, (73), 663.

82 G. M. Badger and I. S. Walker, Polynuclear heterocyclic systems. Part IX. n-π-Transitions in the spectra of aromatic aza-hydrocarbons, *J. Chem. Soc.*, 1951, **3199**, 122.

83 K. Yamamoto, T. Takemura and H. Baba, Fluorescence and dual phosphorescence spectra of Quinoxaline in fluid solution, *Bull. Chem. Soc. Jpn.*, 1978, **51**, 729.

84 H. Patterson and P. Salvi, Poly[tris-(2-amino-butan-1-ol) copper(II) [hexa-kis-μ2-cyanido-κ12C: N-tetra-copper(I)] bis-(2-amino-butan-1-olato)aqua-copper(II) monohydrate], *Inorg. Chem.*, 2024, **9**(8), x240845.

85 C. A. Bayse, T. P. Brewster and R. D. Pike, Photoluminescence of 1-D Copper(I) Cyanide Chains: A Theoretical Description, *Inorg. Chem.*, 2009, **48**(1), 174.

86 G.-Q. Zhong, D. Li and Z.-P. Zhang, Hydrothermal Synthesis, Crystal Structure and Magnetic Property of a Homo-dinuclear Ternary Coordination Polymer of Nickel (II), *Polyhedron*, 2016, **111**, 11.

87 I. Perez, E. S. Larrea, B. Bazán, G. Barandika, M. K. Urtiaga and M. I. Arriortua, Ionothermal Synthesis of Cadmium Coordination Polymers: Ionic Liquid Effects on the Synthesis, Structural, and Thermal Characterization, *Molecules*, 2019, **24**(22), 4059.

88 S. E. H. Etaiw, D. M. Abd El-Aziz, E. M. Shalaby and I. Elzeny, X-ray Structure of Host-Guest Nanosized Organotin Supramolecular Coordination Polymer Based on Cobalt Cyanide and Quinoxaline as an Efficient Catalyst for Treatment of Wastewater, *Appl. Organomet. Chem.*, 2020, **34**(4), e5521.

89 W. H. Glaze, J.-W. Kang and D. H. Chapin, The Chemistry of Water Treatment Processes Involving Ozone, Hydrogen Peroxide and Ultraviolet Radiation, *Ozone: Sci. Eng.*, 1987, **9**(4), 335.

90 B. C. Y. Lee, F. Y. Lim, W. H. Loh, S. L. Ong and J. Hu, Emerging Contaminants: An Overview of Recent Trends for Their Treatment and Management Using Light-Driven Processes, *Water*, 2021, **13**(17), 2340.

91 K. Dutta, S. Bhattacharjee, B. Chaudhuri and S. Mukhopadhyay, Chemical oxidation of methylene blue using a Fenton-like reaction, *J. Environ. Monit.*, 2001, **84**(1), 754.

92 C. H. Wu, C. H. Lai and W. Y. Chung, Electrical Energy per Order and Photodegradation Efficiency of Advanced Oxidation Processes, *Appl. Mech. Mater.*, 2013, **291–294**, 764.

93 Z. Q. Yu and S. S. C. Chuang, Probing Methylene Blue Photocatalytic Degradation by Adsorbed Ethanol with In Situ IR, *J. Phys. Chem. C*, 2007, **111**(37), 13813.

94 A. F. H. Machado, J. A. de Miranda, R. F. de Freitas, E. T. F. M. Duarte, L. F. Ferreira, Y. D. T. Albuquerque, R. Ruggiero, C. Sattler and L. de Oliveira, Destruction of the Organic Matter Present in Effluent from a Cellulose and Paper Industry Using Photocatalysis, *J. Photochem. Photobiol., A*, 2003, **15**, 231.

95 C. Yogi, K. Kojima, N. Wada, H. Tokumoto, T. Takai, T. Mizoguchi and H. Tamiaki, Photocatalytic Degradation of Methylene Blue by TiO_2 Film and Au Particles-TiO_2 Composite Film, *Thin Solid Films*, 2008, **516**(17), 5881.

96 S. E. H. Etaiw, T. A. Fayed, D. M. A. El-Aziz and H. M. Khattab, Self-Assembly and Nano Scaled Ni(II) Coordination Complex as an Efficient Catalyst and Luminescent Sensor, *J. Inorg. Organomet. Polym. Mater.*, 2021, **31**(4), 1621.

97 C. Flox, S. Ammar, C. Arias, E. Brillas, A. Vargas-Zavala and R. Abdelhadi, Electro-Fenton and Photoelectro-Fenton Degradation of Indigo Carmine in Acidic Aqueous Medium, *Appl. Catal., B*, 2006, **67**(1), 93.

98 J. De Laat and T. G. Le, Effects of Chloride Ions on the Iron(III)-Catalyzed Decomposition of Hydrogen Peroxide and on the Efficiency of the Fenton-like Oxidation Process, *Appl. Catal., B*, 2006, **66**(1–2), 137.

99 S. E. H. Etaiw and H. Marie, Two New Ni(II) Supramolecular Complexes Based on Ethyl Isonicotinate and Ethyl Nicotinate for Removal of Acid Blue 92 Dye, *Solid State Sci.*, 2018, **77**, 5.

100 G. Chelucci and R. P. Thummel, Chiral 2, 2'-Bipyridines, 1, 10-Phenanthrolines, and 2, 2': 6', 2' '-Terpyridines: Syntheses and Applications in Asymmetric Homogeneous Catalysis, *Chem. Rev.*, 2002, **102**(9), 3129.

101 X. Q. Wang, D. D. Feng, Y. D. Zhao, D. D. Fang, J. Tang, L. M. Fan and J. A. Yang, Multifunctional 1D Cd-Based Metal-Organic Complex for the Highly Luminescent

Sensitive Detection of Fe^{3+}, $CrO_4^{2-}/Cr_2O_7^{2-}$, and Nitroaromatic Explosives, *J. Solid State Chem.*, 2019, **274**, 40.

102 L. L. Ren, Y. Y. Cui, A. L. Cheng and E. Q. Gao, Water-stable lanthanide-based metal-organic frameworks for rapid and sensitive detection of nitrobenzene derivatives, *J. Solid State Chem.*, 2019, **270**, 463.

103 J. Przybyla and R. L. LaDuca, Nitrobenzene-detection cadmium thiophenedicarboxylate coordination polymers with flexible dipyridylamide ligands and diverse topologies, *Inorg. Chim. Acta*, 2019, **486**, 314.

104 G. A. Farnum, B. L. Martinez, J. L. Meyer, S. R. Pumford and R. L. LaDuca, Diverse stacked and entangled topologies in cadmium tricarballylate coordination polymers with nitrobenzene detection capability, *Inorg. Chim. Acta*, 2019, **485**, 9.

105 Y.-Q. Zhang, V. A. Blatov, T.-R. Zheng, C.-H. Yang, L.-L. Qian, K. Li, B.-L. Li and B. Wu, Iron(III) identification and proton conductionof a luminescent metal-organic framework, *Dalton Trans.*, 2018, **47**, 6189.

106 X.-X. Wang, X.-Q. Wang, X.-Y. Niu and T.-P. Hu, Two Chemically Stable Cd(II) Polymers as Fluorescent Sensor and Photocatalyst for Aromatic Dyes, *Cryst. Eng. Commun.*, 2016, **18**, 7471.

107 A. Buragohain, M. Yousufuddin, M. Sarma and S. Biswas, 3D Luminescent Amide-Functionalized Cadmium Tetrazolate Framework for Selective Detection of 2, 4, 6-Trinitrophenol, *Cryst. Growth Des.*, 2016, **16**, 842.

108 U. S. Department of Health and Human Services, *Toxicological Profile for Chromium*, Public Health Service Agency for Toxic Substances and Disease Registry, Atlanta, GA, 1991.

109 W.-X. Li, H.-X. Li, H.-Y. Li, M.-M. Chen, Y.-X. Shi and J.-P. Lang, Selective recognition of Hg2+ ions in aqueous solution by a Cd^{II}-based metal-organic framework with good stability and vacant coordination sites, *Cryst. Growth Des.*, 2017, **17**, 3948.

110 Y. Rachuri, B. Parmar, K. K. Bisht and E. Suresh, Mixed ligand two-dimensional Cd(ii)/Ni(ii) metal organic frameworks containing dicarboxylate and tripodal N-donor ligands: Cd(ii) MOF is an efficient luminescent sensor for detection of picric acid in aqueous media, *Dalton Trans.*, 2016, **45**, 7881.

111 H. Wang, F. Cheng, C. Zou, Q. Li, Y. Hua, J. Duan and W. Jin, A luminescent Cd(II) coordination polymer based on flexible bis(pyridyl) ligands: synthesis, crystal structure, and sensing properties, *Cryst. Eng. Commun.*, 2016, **18**, 5639.

112 H. Xu, J. Gao, X. Qian, J. Wang, H. He, Y. Cui, Y. Yang, Z. Wang and G. A. Qian, luminescent metal-organic framework for highly sensitive and selective detection of nitroaromatic explosives, *J. Mater. Chem. A*, 2016, **4**, 10900.

113 X. R. Wang, X. Z. Wang, Y. Li, K. Liu, S. X. Liu, J. Du, Z. Huang, Y. Luo, J. Z. Huo and X. X. Wu, Four Coordination Polymers Luminescent Materials for Selectively Detection of $Fe^{3+}/Cr_2O_7^{2-}$/Nitrobenzene in Solution Phase, *J. Solid State Chem.*, 2022, **315**, 123523.

114 L. T. Popoola, A. S. Yusuff, A. T. Adejare and S. B. Olasupo, Photocatalytic degradation of methylene blue dye by magnetized TiO2-silica nanoparticles from rice husk, *Appl. Water Sci.*, 2024, **14**(2), 25, DOI: **10.1007/s13201-023-02052-8**.

115 M. H. Dehghani Popoola, S. Ahmadi Aderibigbe, S. Ghosh Yusuff, A. Othmani, C. Osagie, M Meskini, S. AlKafaas, A. Malloum, W. Khanday, O. Jacob, Ö Gökkuş, A. Oroke, O. Martins Chineme, R. R. Karr and E. C. Lima, Recent Advances on Sustainable Adsorbents for the Remediation of Noxious Pollutants from Water and Wastewater: A Critical Review, *Arabian J. Chem.*, 2023, **16**(12), 105303–105378, DOI: **10.1016/j.arabjc.2023.105303.1**.

116 S. Balu, D. Ganapathy, S. Arya, R. Atchudan and A. K. Sundramoorthy, Advanced photocatalytic materials based degradation of micropollutants and their use in hydrogen production – a review, *RSC Adv.*, 2024, **14**(20), 14392–14424, DOI: **10.1039/D4RA01307G**.

117 A. K. Nair, D. Roy George, N. Jos Baby, M. Reji and S. Joseph, Solar dye degradation using TiO2 nanosheet based nanocomposite floating photocatalyst, *Mater. Today: Proc.*, 2023, **46**, 2747–2751, DOI: **10.1016/j.matpr.2021.02.481**.

118 M. N. Rashed, M. A. Eltaher and A. N. A. Abdou, Adsorption and photocatalysis for methyl orange and Cd removal from wastewater using TiO_2/sewage sludge-based activated carbon nanocomposites, *R. Soc. Open Sci.*, 2017, **4**(12), 170834, DOI: **10.1098/rsos.170834**.

119 G. Chandrabose, A. Dey, S. S. Gaur, S. Pitchaimuthu, H Jagadeesan, N. S. J. Braithwaite, V. Selvaraj, V. Kumar and S. Krishnamurthy, Removal and degradation of mixed dye pollutants by integrated adsorption-photocatalysis technique using 2-D MoS_2/TiO_2 nanocomposite, *Chemosphere*, 2021, **279**, 130467, DOI: **10.1016/j.chemosphere.2021.130467**.

120 S. Mishra, N. Chakinala, A. G. Chakinala and P. K. Surolia, Photocatalytic degradation of methylene blue using monometallic and bimetallic Bi-Fe doped TiO2, *Catal. Commun.*, 2022, **171**, 106518, DOI: **10.1016/j.catcom.2022.106518**.

121 Z. Kalaycıoğlu, B. Özuğur Uysal, Ö. Pekcan and F. B. Erim, Efficient Photocatalytic Degradation of Methylene Blue Dye from Aqueous Solution with Cerium Oxide Nanoparticles and Graphene Oxide-Doped Polyacrylamide, *ACS Omega*, 2023, **8**(14), 13004–13015, DOI: **10.1021/acsomega.3c00198**.

122 P. Ngwenya, F. A. Bezza, M. Tichapondwa Shepherd and M. N. Chirwa Evans, Photocatalytic Degradation of Brilliant Green Dye using B-TiO2 under Visible Light Irradiation, *Chem. Eng. Trans.*, 2025, **117**, 361–366, DOI: **10.3303/CET25117061**.

123 A. S. Yusuff, Photocatalytic Degradation of Cationic Dye in Aqueous Solution by TiO_2 Nanoparticle Immobilized on Termite Hill Soil, *React. Kinet., Mech. Catal.*, 2020, **131**(2), 979, DOI: **10.1007/s11144-020-01883-9**.

124 O. Długosz, A. Staroń, P. Brzoza and M. Banach, Synergistic effect of sorption and photocatalysis on the degree of dye removal in single and multicomponent systems on ZnO-

SnO2, *Environ. Sci. Pollut. Res.*, 2022, **29**(18), 27042–27050, DOI: **10.1007/s11356-021-18044-7**.

125 L. T. Popoola, T. A. Aderibigbe, A. S. Yusuff and M. M. Munir, Brilliant green dye adsorption onto composite snail shell–rice husk: Adsorption isotherm, kinetic, mechanistic, and thermodynamics analysis, *Environ. Qual. Manage.*, 2018, **28**(2), 63–78, DOI: **10.1002/tqem.21597**.

126 A. Zyoud, M. Ateeq, M. H. Helal, S. H. Zyoud and H. S. Hilal, Photocatalytic Degradation of Phenazopyridine Contaminant in Soil with Direct Solar Light, *Environ. Technol.*, 2019, **40**(22), 2928, DOI: **10.1080/09593330.2018.1459873**.

127 N. M. El Kawas, A. H. Zaki and M. Taha, Methylene Blue and Methyl Orange Removal Using Green Rust as a Low-Cost, Sustainable Adsorbent and Photocatalyst, *RSC Adv.*, 2025, **15**(23), 18403, DOI: **10.1039/D5RA01508A**.

128 K. Nagendra Naik, K. Yogendra and K. M. Mahadeva, Solar Light Induced Photodegradation of Brilliant Green Dye by Barium Calciate ($BaCaO_2$) Nanoparticles, *Nat., Environ. Pollut. Technol.*, 2020, **19**(4), 1683, DOI: **10.46488/NEPT.2020.v19i04.037**.

129 G. Chandrabose, A. Dey, S. S. Gaur, S. Pitchaimuthu, H. Jagadeesan, N. S. J. Braithwaite, V. Selvaraj, V. Kumar and S. Krishnamurthy, Removal and degradation of mixed dye pollutants by integrated adsorption-photocatalysis technique using 2-D MoS2/TiO2 composite, *Chemosphere*, 2021, **279**, 130467.

130 Z. Kalaycıoğlu, B. Özuğur Uysal, Ö. Pekcan and F. B. Erim, Efficient Photocatalytic Degradation of Methylene Blue Dye from Aqueous Solution with Cerium Oxide Nanoparticles and Graphene Oxide-Doped Polyacrylamide, *ACS Omega*, 2023, **8**(14), 13004, DOI: **10.1021/acsomega.3c00198**.